AIAA JOURNAL
Vol. 50, No. 5, May 2012

Numerical Dissipation Effects on Massive Separation Around Tandem Cylinders

Zhixiang Xiao,* Jian Liu,† Jingbo Huang,‡ and Song Fu§
Tsinghua University, 100084 Beijing, People's Republic of China

DOI: 10.2514/1.J051299

Three spatial schemes, the original Roe scheme and two high-order symmetric total variation diminishing schemes, whose dissipations are multiplied by a constant parameter or a function (called ϕ), are coupled with delayed detached eddy simulation to investigate the numerical dissipation effects on the massive separation flow around tandem cylinders. From the comparisons between the computations and the available measurements, the numerical dissipation has a significant influence on the mean and instantaneous flowfields. The original Roe scheme is too dissipative to predict the small scale turbulent structures, and it strongly suppresses the growth of resolved turbulence. The S6WENO5 schemes with constant-ϕ and adaptive-ϕ times of dissipation have similar performances and they well match the measurements. However, the S6WENO5 with constant-ϕ times (0.12 here) of dissipation is too empirical, and the small constant-ϕ times of dissipation cannot generally suppress the numerical oscillations near the wall and in the far fields. The S6WENO5 with adaptive dissipation provides the best performance.

Nomenclature

A	=	variable in blending function of adaptive dissipation
$\tilde{A}_{\text{inv}}$	=	matrix of Roe average
B	=	variable in blending function of adaptive dissipation
C_D	=	coefficient of drag
C_{DES}	=	constant of detached eddy simulation or delayed detached eddy simulation
$C_{\text{DES},k\text{-}\omega}$	=	constant of k-ω part in delayed detached eddy simulation
$C_{\text{DES},k\text{-}\varepsilon}$	=	constant of k-ε part in delayed detached eddy simulation
CH1	=	constant in blending function of adaptive dissipation
CH2	=	constant in blending function of adaptive dissipation
CH3	=	constant in blending function of adaptive dissipation
C_L	=	coefficient of lift
C_p	=	coefficient of pressure
$C_{p,\text{rms}}$	=	root mean square of pressure coefficient
C_μ	=	constant in blending function of adaptive dissipation
D	=	diameter of cylinder
F	=	inviscid flux of Navier–Stokes equations
F_{DES}	=	hybrid function in delayed detached eddy simulation
F_{SST}	=	blending function in delayed detached eddy simulation
F_1 or F_2	=	blending function in shear stress transport model
g	=	variable in blending function of adaptive dissipation
K	=	variable in blending function of adaptive dissipation
k	=	turbulence kinetic energy
$k'(4)$	=	coefficient of fourth artificial viscosity
L	=	space of two cylinders
L_{nond}	=	nondimensional unit length
L_t	=	turbulent length scale in delayed detached eddy simulation
L_{turb}	=	length scale of turbulence in blending function of adaptive dissipation
q^L and q^R	=	left and right biased original variables in Navier–Stokes equations
$\tilde{S}$	=	magnitude of mean strain rate
S_{ij}	=	tensor of strain rate
t	=	time
U_0	=	freestream velocity
$u_{i,j,k}$	=	components of velocity in x, y and z directions, respectively
W_{ij}	=	tensor of vorticity
$x_{i,j,k}$	=	components of coordinates (x, y and z)
β^*	=	constant of turbulent kinetic energy equation
Δ	=	grid scale
Δz	=	interval in spanwise direction
$\mu_{L,T}$	=	laminar or turbulent viscosity
$\nu_{L,T}$	=	laminar or turbulent molecular viscosity
ρ	=	density
σ_k	=	constant of turbulent kinetic energy equation
τ	=	time scale in blending function of adaptive dissipation
τ_{ij}	=	tensor of Reynolds stress
ϕ	=	parameter of numerical dissipation in Roe or symmetric total variation diminishing scheme
Ω	=	magnitude of vorticity
ω	=	specific dissipative rate

Subscripts

i, j, k	=	at grid center
$i + 1/2$	=	at right interface of cell 1 in i-direction

Received 30 March 2011; revision received 21 October 2011; accepted for publication 22 October 2011.

*Associate Professor, School of Aerospace Engineering. Senior Member AIAA.
†M.Sc. Student, School of Aerospace Engineering.
‡Post-Doctor, School of Aerospace Engineering. Member AIAA.
§Professor, School of Aerospace Engineering; fs-dem@tsinghua.edu.cn. Associate Fellow AIAA (Corresponding Author).

I. Introduction

TURBULENCE dominates the unsteady flows past the civil transporters in the flight stages of taking off and landing, especially when the landing gears intrude into the air. The flow around the landing gear is extremely complex and massively separated, and turbulence plays an important role affecting

aeroacoustics through pressure fluctuation. Highly accurate and efficient analytical tools are required to simulate these strongly unsteady and wide frequency separation flows. These tools help the designer to control these massive and unsteady separations, to improve the aircraft's performance and to decrease the airframe noise.

Lazos designed a simplified landing gear (SLG) with four wheels and necessary struts, scaled to the main landing gear of a Boeing 757. Mean surface pressure [1], surface flow topology [2], and Reynolds stresses [3] were presented, and they could be used to validate the computational fluid dynamics (CFD) tools. However, the SLG's geometry is also relatively complex, it is difficult to explore the unsteady flow features and to distinguish the contributions of SLG's components.

The tandem cylinder (TC) is a prototype for interaction problems commonly encountered in airframe noise configurations (e.g., the oleo and hoses of a landing gear). Measurements of the unsteady flow around the TC as well as aeroacoustic experiments on both cylinder surfaces and in the far field were conducted in NASA Langley Research Center [4–6]. The TC configuration is also one of the test cases in the European Seventh Framework project Advanced Turbulence Simulation for Aerodynamic Application Challenges (ATAAC [7]) and the AIAA Workshop on Benchmark Problems for Airframe Noise Computations (BANC [8,9]). In fact, there have been concentrated numerical studies in recent years focusing on the turbulence behavior of the flows around TC.

Khorrami et al. [10], Lockard et al. [11], and Khorrami et al. [12] computed the flows past TC, with the spacing (L) of the two cylinder centers at 3.7 [10–12] and 1.435 [10,12,13] diameters (D), respectively, with a quasi-laminar and zonal approach. They investigated the effects of the spanwise length on the mean flows, such as pressure distribution, velocity, and turbulence kinetic energy, and on the unsteady flows, such as instantaneous spanwise vorticities and pressure fluctuation. The sound pressure levels were analyzed through the unsteady pressure fluctuation data. At the same time, they point out that "Presently, we do not have a rule of thumb on how to arrive at an optimal width for the turbulent zone. The current width was selected based on our past experiences with similar issues involving high-lift flow computations and a desire to keep the preseparated boundary layers on the cylinders immersed within the fully turbulent zone" [10].

Brès et al. [14,15] calculated the flow past TC of the spacing at $3.7D$ with the Lattice–Boltzmann method. Highly effective and reasonable mean flowfields can be obtained when comparing with the measurements. They also investigated the effect of the spanwise domain with and without end plates. They found that the end plates have an important influence on the spanwise correlation.

Weinmann et al. [16] studied the same flow with a number of novel Reynolds-averaged Navier–Stokes/large eddy simulation (RANS/LES) hybrid methods, such as improved delayed detached eddy simulation (IDDES), flow simulation methodology and scale adaptive simulation based on an explicit algebraic Reynolds stress model. Most of the mean flows agreed reasonably well with the measurements, but the instantaneous turbulence structures appeared somewhat excessively large and strong causing the root mean square (RMS) of the pressure coefficient ($C_{p,\mathrm{rms}}$) on the front cylinder overpredicted. They analyzed that "By increasing the spanwise extent and the number of grid cells in the spanwise direction, they were able to reduce the overall level of pressure fluctuations on the first cylinder."

According to the references cited previously and the experience of the present work, in order to accurately simulate the flows past TC with massively unsteady separation, two issues should be addressed: appropriate turbulence modeling and acceptable numerical dissipation.

A. Highly Accurate and Efficient RANS/LES Hybrid Methods

The most accurate turbulence model can be attributed to the direct numerical simulation (DNS). All the turbulence scales are directly resolved both in time and space. It requires the spatial and temporal resolution sufficient to predict the smallest motions. DNS is thus the most expensive turbulence prediction approach, which is impossible to be applied to the high Reynolds number flows in the recent years. Spalart [17] estimated that the first DNS application to a complete aircraft could be realized only after 2080.

LES is a powerful tool for resolving the large, energy-containing scale motions that are typically time dependent and geometry dependent. The reduction in the computational cost as compared with DNS is through introducing some empiricism. The large energy-containing scale motions are directly computed while the relatively isotropic and universal scale motions are modeled using the subgrid scale (SGS) model. Still, SGS models for the boundary layer and compressible flows are not sufficiently well developed. In fact, LES requires almost similar grid numbers as DNS for high Reynolds number flows near the wall, indicating that LES is equally expensive as DNS in these regions.

Although there are many unanswered questions including the turbulence modeling uncertainty, solving RANS equations with various turbulence models are widely employed as appropriate aerovehicles design approach. The RANS approach had been developed to predict many of the important mean flow characteristics, such as the force, moment, velocity, and so on, but it was not intended to simulate the complex unsteady flows, nor pressure fluctuations. Unsteady RANS (URANS) is not a satisfactory approach to investigate unsteady turbulence behavior; the large time steps and high-level eddy viscosity always eliminate high-frequency small scale motions.

Limited by computational resources, the combination of LES with RANS can achieve reasonably well in terms of both efficiency and accuracy in computing the flows with massive separation. The modeling strategy of turbulent flows, often referred to as RANS/LES hybrid models (such as DES, originally proposed by Spalart et al. [18], denoted as DES97), has recently become much favored in the study of the unsteady and geometry-dependent separated flows. Such hybrid methods combine a high-efficiency turbulence model near the wall, where the flow is dominated by small scale motions, with a LES-type treatment for the large-scale motions in the flow region far away from the wall. The original DES based on Spalart–Allmaras (SA) model [19] achieved widespread acceptance in industrial CFD community. However, some inherent shortcomings are identified with the DES97 from its outset and some others are demonstrated through further investigation. These shortcomings include erroneous activities of the near wall damping terms in LES mode, incursion of LES mode inside boundary layer, gray area and log-layer mismatch. Many of these have been successfully addressed in the later revisions (DDES [20], IDDES [21], extended DDES [22]) and some remain.

Strelets [23] proposed the first DES based on the two-equation shear-stress transport (SST) model [24]. This SST-based DES (or SST-DES) has, undesirably, the similar deficiency as the original SA-DES, for instance, the separation can be induced by local clustered grid indicating that the LES mode acts inside boundary layer. Menter and Kuntz [25] observed the separation around an airfoil trailing edge in SST-DES results more upstream than that by SST-RANS. The SST-DES is thus seen to give what is called "grid induced separation." To prevent this unwanted separation, a shield function was used to disable the LES mode in the attached boundary layer. The modified version of SST-DES is named as SST-delayed-DES, or SST-DDES in short. The present authors also observed the horseshoe separation before the Rood wing–body junction [26] and the vortex breakdown past a wing–fuselage at a moderate angle of attack [27] with SST-DES more upstream than those of measurements and URANS. When SST-DDES was applied to calculate the preceding two cases, significant improvements in the mean pressure coefficients, velocity profiles and Reynolds stress profiles were achieved.

B. Low-Dissipation Numerical Schemes

Another noticeable issue is the numerical dissipation associated with the discretization scheme for the convective terms of NS equations adopted in the computation. Large numerical dissipation is likely to contaminate and even overshadow the physical viscosity. In

that case only very large-scale unsteady vortices can be resolved and most of the small scale turbulence structures are eliminated by the numerical dissipation. This numerical issue has not be fully recognized, however, there are still plenty of references exhibiting results obtained with the DES-type methods coupled with some low-order upwind schemes even in the very recent years. But more and more people now realize the deficiency of the upwind discretization scheme and make very good effort in eliminating the negative effect of the numerical dissipation to provide accurate numerical results. Three types of efforts can be classified as 1) increasing the discretization order of the scheme, 2) reducing the numerical dissipation, or 3) both:

1) Xiao and Fu [28] investigated three types of afterbodies in an attempt to highlight the influences on drag reduction using SST-DES with fifth-order weighted essential nonoscillatory (WENO) interpolation based on the approximate Riemann solver of the Roe scheme. Wang et al. [29] investigated the nonlinearity of the fluid–structural interaction with SA-RANS and SA-DES through a low-diffusion total energy-convective upwind and split pressure scheme with the fifth-order WENO scheme.

2) Bui [30] reduced the dissipation of the upwind Roe scheme with third monotone upstream-central schemes for conservation laws (MUSCL) interpolation by multiplying a small constant (ϕ), ranging from 0.03 to 0.05, to calculate the fully developed turbulence in a square duct with LES. This approach is simple and easy to implement, but it is too empirical and lacks physics. If it is applied to simulate the strong shear layer or flows with strong adverse pressure gradients, it becomes numerically unstable and easily diverged. Qin and Xia [31] reduced the numerical dissipation of the Roe scheme in the same way to predict the synthetic jet flow. To obtain the balance of numerical accuracy and stability, the constant ϕ is taken as 0.4, which is much larger than that of Bui. Yoon and Barnhardt [32] tried to explore the transition mechanism past a single roughness element with a combination of DES and a modified low-dissipation version of the Steger and Warming scheme.

3) The natural choice for the numerical scheme of LES and LES/RANS hybrid approaches is the central-type schemes. However, the purely central schemes suffer from the numerical instability. Therefore, high-order central schemes with low dissipation are much preferred in LES/RANS hybrid models. In fact, the combination of the central and upwind scheme [23,33], fifth order in space and second order in time, had been smartly designed to accurately predict the turbulence. This upwind/central hybrid scheme functions as an effectively central scheme in the separated regions where DES is operating in an LES mode, and as an upwind-biased scheme near the wall (RANS mode) and in the outer irrotational regions.

In this paper, we mainly investigate and discuss the effect of dissipation of the symmetric total variation diminishing (STVD) scheme on the turbulence simulation coupled with SST-DDES methods. Roe scheme with third MUSCL interpolation is applied to compare with the other two STVD schemes with constant (0.12) and adaptive dissipation dependent on the flow.

II. Spatial Schemes with Low Dissipation

When LES is applied to simulate turbulent flows, the numerical dissipation should be low enough with very fine grid resolutions to resolve the appropriate turbulence scales. High-order central schemes are frequently used; however, they often suffer from spurious oscillations with coarse grids at the far-field boundary and near the wall where the upwind scheme or relatively large dissipation may be required. In the present work, three spatial schemes, the central/upwind hybrid scheme, the upwind scheme with simple and direct dissipation reduction, and the modified STVD with controllable dispersion and dissipation errors, are compared and analyzed in the similar formulations.

A. Central/Upwind Hybrid Scheme

Strelets [23] and Travin et al. [33] proposed a central/upwind hybrid approximate inviscid scheme; it can be given as

$$F_{i+1/2} = (1-\phi)F_{\text{central},i+1/2} + \phi F_{\text{upwind},i+1/2} \tag{1}$$

where F is the inviscid flux; $F_{\text{central},i+1/2}$ and $F_{\text{upwind},i+1/2}$ denote, respectively, the central (fourth-order) and upwind (third- or fifth-order) approximation of inviscid flux, which are easily constructed; and parameter ϕ is a blending function. This function becomes its maximum value of 1.0, resulting in an "almost upwind" scheme, near the wall where RANS mode acts and in the irrotational region of the flow to guarantee stability of the scheme with the coarse grids. It is close to zero in the LES region, resulting in an "almost central" scheme to well resolve the small scale of turbulence structures.

1. Formulation of Blending Function ϕ

Here, the construction of the blending function is crucially important for accurate simulation of turbulence. In the original formulation of Strelets [23] and Travin et al. [33] some typographical errors are found; after careful analysis and comparison with relevant [34], the modified blending function is given as

$$\phi = \phi_{\max}\tanh(A^{\text{CH1}}) \tag{2}$$

where $A = \text{CH2}\cdot\max\{[C_{\text{DES}}\Delta/L_{\text{turb}}/g - 0.5]; 0\}$, $L_{\text{turb}} = [(v_T + v_L)/(C_\mu^{3/2}K)]^{1/2}$, $K = \max\{[(\tilde{S}^2 + \Omega^2)/2]^{1/2}; 0.1\tau^{-1}\}$, $\tau = L_{\text{nond}}/U_0$, $g = \tanh(B^4)$, and $B = \text{CH3}\cdot\Omega\cdot\max(\Omega, \tilde{S})/\max[(\tilde{S}^2 + \Omega^2)/2, 10^{-20}]$. The constants are given as: $\phi_{\max} = 1$, $\text{CH1} = 3$, $\text{CH2} = 1$, and $\text{CH3} = 2$; C_{DES} is recalibrated in our in-house code UNITs (which stands for "unsteady Navier–Stokes equation solver") and determined in the well-established case of decaying isotropic turbulence (DIT). The values are given in Sec. V. Δ is the grid length scale defined as $\Delta = \max(\Delta x, \Delta y, \Delta z)$. $\Omega = (2W_{ij}W_{ji})^{0.5}$ and $\tilde{S} = (2S_{ij}S_{ji})^{0.5}$, where $S_{ij} = (\partial u_i/\partial x_j + \partial u_j/\partial x_i)/2$ and $W_{ij} = (\partial u_i/\partial x_j - \partial u_j/\partial x_i)/2$.

2. Analysis of Blending Function ϕ

As shown in Eq. (2), the blending function is in the hyperbolic tangent form; $\tanh(x)$ roughly reaches one when the independent variable x is about two, shown in Fig. 1.

In the irrotational region, where $\tilde{S}$ can be significant while Ω is very small, variable B becomes a very small value and the variable g will also be small. Thus, the variable A becomes very large and the blending function ϕ reaches one. In this case, the central/upwind scheme acts as an upwind one.

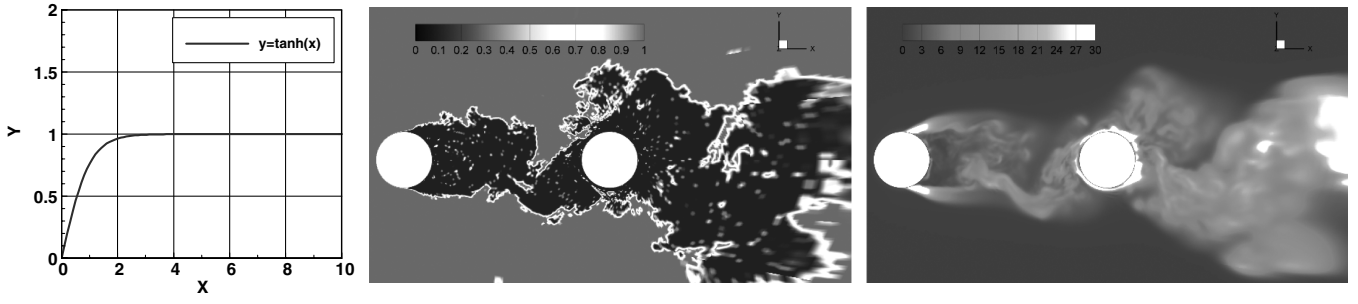

Fig. 1 The property of $y = \tanh(x)$, the snapshot of the function ϕ (middle) and the modeled eddy viscosity (right).

In the separation region, Ω and $\tilde{S}$ are in the same order of magnitude, variable B^4 will be likely greater than two, and the variable g then goes to one. The variable A is here only determined by grid scale ($C_{\mathrm{DES}}\Delta$) and turbulence scale. In the separated region dominated by turbulence, the eddy viscosity is very significant, indicating that the turbulent scale L_{turb} is very large as compared to the grid scales, which are very small. Therefore, the ratio of $(C_{\mathrm{DES}}\Delta)/L_{\mathrm{turb}}$ will be less than 0.5. The variable A is here very small and negligible. The central/upwind scheme acts as a central one.

Near the wall, Ω and $\tilde{S}$ are very large and have the same order of magnitude. The variable A is dominated by the ratio of the grid to the turbulence length scales. In fact, the grid scales are much larger than the turbulence scales, causing the variable A to be large. The blending function ϕ will then be unity and the central/upwind scheme converts again to the upwind one.

As shown in Fig. 1, the function ϕ approaches zero in the recirculation region where the flow is dominated by turbulence and the scheme acts as in the central mode. Conversely, in the near wall and in the irrotational region, the blending function ϕ is close to one and the scheme is practically the upwind model.

B. Modified Roe Scheme

The inviscid flux of the Roe scheme is given as

$$F_{i+1/2} = \frac{1}{2}[F(q^L) + F(q^R)]_{i+1/2} - \phi \times \frac{1}{2}|\tilde{A}_{\mathrm{inv}}|(q^R - q^L)_{i+1/2} \quad (3)$$

where q^L and q^R are the original variables at the left- and right-hand sides of the interface $(\,)_{i+1/2}$ reconstructed by third-order MUSCL or fifth-order WENO [35] interpolation; $\tilde{A}_{\mathrm{inv}}$ is the matrix of Roe averaged. In the original Roe scheme, the parameter ϕ is taken as one.

To reduce the dissipation of the upwind scheme effectively and directly, parameter ϕ is taken as 0.03–0.05 [30] and 0.4 [31], respectively. If we rearrange the flux and dissipation terms of Eq. (3), it can then be written as

$$\begin{aligned} F_{i+1/2} &= (1-\phi) \times \frac{1}{2}[F(q^L) + F(q^R)]_{i+1/2} + \phi \times \left\{\frac{1}{2}[F(q^L) \right. \\ &\quad \left. + F(q^R)]_{i+1/2} - \frac{1}{2}|\tilde{A}_{\mathrm{inv}}|(q^R - q^L)_{i+1/2}\right\} \\ &= (1-\phi) \times \frac{1}{2}[F(q^L) + F(q^R)]_{i+1/2} + \phi \times F_{\mathrm{upwind},i+1/2} \end{aligned} \quad (4)$$

From the preceding equation, the modified low-dissipation Roe scheme looks very similar to the central/upwind scheme in Eq. (1). The only difference is the flux of the central scheme. In fact, this scheme introduces slightly more dissipation than that in Eq. (1), because the left and right fluxes at the interface are achieved with the upwind-biased interpolation.

C. Modified STVD Scheme

The STVD-type scheme was originally proposed by Yee et al. [36]. The idea of STVD is to combine the high-order symmetric difference schemes with relatively lower-order dissipation terms to yield better accuracy. Because STVD is spatially symmetric, it has no inherent dissipation, as does the upwind scheme. In this paper, the reason for choosing STVD schemes is that this algorithm allows one to independently control the dispersion and dissipation errors in the solution [37].

The inviscid flux and the dissipation of the STVD scheme can be written as

$$F_{i+1/2} = \underbrace{F_{\mathrm{symmetric},i+1/2}}_{6^{\mathrm{th}}\ \mathrm{order,symmetric,scheme}} \underbrace{- \phi \times \frac{1}{2}|\tilde{A}_{\mathrm{inv}}|(q^R - q^L)_{i+1/2}}_{5^{\mathrm{th}}\ \mathrm{order,WENO}} \quad (5)$$

where the inviscid flux is in the sixth-order symmetric scheme and given as $F_{\mathrm{symmetric},i+1/2} = (F_{i-2} - 8F_{i-1} + 37F_i + 37F_{i+1} - 8F_{i+2} + F_{i+3})/60$. The numerical dissipation is the original Roe's dissipation with fifth-order WENO interpolation. Then, this STVD scheme can be shortened as S6WENO5. $\tilde{A}_{\mathrm{inv}}$ has the similar formulations as in Eq. (3), and q^R and q^L are obtained through the fifth WENO reconstruction. The parameter ϕ of the original S6WENO5 scheme is taken as one. In this work, ϕ is taken as not only a constant (0.12), but also the blending function in Eq. (2).

After comparing Eqs. (1), (4), and (5), the S6WENO5 scheme contains the symmetric flux with the diffusion terms of the Roe-type upwind scheme. It does not need to compute the upwind fluxes ($F_{\mathrm{upwind},i+1/2}$) and it keeps the original symmetric flux without a coefficient of $(1-\phi)$. Then, its numerical dissipation is dependent on flows and its dispersion is controllable.

III. Formulation of the Hybrid RANS/LES Method: DDES

Here, the fundamental turbulence model is the SST model by proposed Menter [24]. The detailed formulations are omitted here but can be found in many references.

To formulate a DES-type hybrid method based on two-equation k-ω models, modification is required in the destruction term in the turbulent kinetic energy (TKE) transport equation. After introducing the turbulence length scale, the kinetic energy equation can be rewritten as

$$\frac{\partial(\rho k)}{\partial t} + \frac{\partial \rho u_j k}{\partial x_j} = \frac{\partial}{\partial x_j}\left[(\mu + \sigma_k \mu_t)\frac{\partial k}{\partial x_j}\right] + \tau_{ij}S_{ij} - \beta^*\rho k\omega F_{\mathrm{DES}} \quad (6)$$

where F_{DES} is the hybrid function defined as

$$F_{\mathrm{DES}} = \max\left[(1 - F_{\mathrm{SST}}) \cdot \frac{L_t}{C_{\mathrm{DES}}\Delta}; 1\right] \quad (7)$$

and the turbulence length scale L_t is defined as $L_t = k^{1/2}/(\beta^*\omega)$; $C_{\mathrm{DES}} = F_1 \times C_{\mathrm{DES},k\text{-}\omega} + (1 - F_1) \times C_{\mathrm{DES},k\text{-}\varepsilon}$ where the two parts of C_{DES} should be recalibrated using the users' own CFD codes. F_{SST} can be taken as zero, F_1 or F_2, where F_1 and F_2 are two blending functions in SST model. If $F_{\mathrm{SST}} = 0$, the hybrid method reverts to a Strelets-type [23] SST-DES method. If $F_{\mathrm{SST}} = F_1$ or F_2, then, this hybrid approach becomes the delayed-DES method (DDES). Because of the properties of functions F_1 and F_2, $1 - F_{\mathrm{SST}}$ approaches zero near the wall, and the DDES will act in the RANS mode there. Also, if $1 - F_{\mathrm{SST}}$ becomes one outside of the boundary layer, DDES goes back to the original Strelets-type DES model. Thus, DDES can ensure itself to act in the RANS mode near the wall without the effects on the local clustered grid scales. In other words, DDES can delay the LES mode in the boundary layer due to the grid scales, especially the locally refined grids in the streamwise and spanwise direction for the complex configurations. In this paper, F_{SST} is taken as F_2.

The ω-equation and the eddy viscosity definition are the same as that in the SST model. In the Strelets-type DES approach (i.e., $F_{\mathrm{SST}} = 0$), when $L_t/(C_{\mathrm{DES}\Delta}) < 1$, $F_{\mathrm{DES}} = 1$, the hybrid method acts in the RANS mode. When $L_t > C_{\mathrm{DES}}\Delta$, the method acts in the Smagorinsky LES mode. If the turbulence production is in balance with the dissipation term, $P_k = \rho v_t \tilde{S}^2 = D_k = \rho k^{3/2}/L_t$, $k = \beta^* L_t^2 \tilde{S}^2$ and $L_t = C_{\mathrm{DES}}\Delta$, then, the eddy viscosity can be rewritten as

$$v_t = (\beta^*)^{3/2}(C_{\mathrm{DES}}\Delta)^2\tilde{S} \propto \Delta^2\tilde{S} \quad (8)$$

Here, the eddy viscosity is similar to that defined in Smagorinsky's model. When the grid is locally refined, the hybrid method will act as in a LES mode.

It should be pointed out that the present DDES (2003) and Spalart's DDES (2006) are based on different fundamental turbulence models and the different shield functions. DDES by Spalart is based on the one-equation SA model, while the present DDES is on the two-equation SST model. Nevertheless, the two versions of DDES perform almost the same. The difference and relationship between versions 2003 and 2006 have been investigated by the

authors [38] and the shield function has an important influence on their performance.

IV. Other Numerical Methods

The in-house code of UNITs, which is in a cell-central finite volume formulation based on multiblock structured grids, is applied to validate the spatial schemes and turbulence modeling method. A modified fully implicit lower–upper symmetric Gauss–Seidel (LU-SGS) with Newton-like subiteration in pseudotime is taken as the time marching method when solving the NS and the turbulence model equations. The approach is in a parallel algorithm using domain-decomposition and message-passing-interface strategies for the platform on computer clusters.

Because our in-house code is a compressible solver, in order to capture the shock wave, some limiters are introduced in the original Roe scheme, shown in Eq. (3), when the original variables of mean NS equations are reconstructed using the third MUSCL interpolation. In this paper, the limiter is given in Eq. (9):

$$(q^L)_{i+1/2} = q_i + \frac{1}{2}\text{limiter}(q_{i+1} - q_i, q_i - q_{i-1})$$

$$(q^R)_{i+1/2} = q_{i+1} - \frac{1}{2}\text{limiter}(q_i - q_{i-1}, q_{i+1} - q_i)$$

$$\text{limiter}(x, y) = \frac{x(y^2 + 2\varepsilon^2) + y(2x^2 + \varepsilon^2)}{2x^2 - xy + 2y^2 + 3\varepsilon^2} \tag{9}$$

where ε is a very small constant, about 1×10^{-6}.

At the same time, the Radespiel and Swanson [39] entropy fix was also applied in the convective terms of NS equations to avoid the unphysical oscillation when the eigenvalues of the NS equations approach zero at the sound speed and stagnation.

The TKE and specific dissipation rate transport equations are solved, decoupled with the mean flow equations using LU-SGS method with subiterations. The production terms are treated explicitly, lagged in time whereas the destruction and diffusion terms are treated implicitly (they are linearized and a term is brought to the left-hand side of the equations). Treating the destruction terms implicitly helps increase the diagonal dominance of the left-hand-side matrix.

The computation of DDES starts from initial flowfields obtained by solving URANS equations. The time-averaged flow is obtained through averaging several relatively regular vortex shedding periods.

V. Results and Discussions

In this section, two test cases are applied to explore the effects of numerical dissipation on the turbulence behavior and flow features. All the turbulence simulation methods are SST-DDES (2003). The appropriate spatial scheme in combination with the DDES formulation also in the present work will be recommended as a result of this study.

A. Decaying Isotropic Turbulence

DIT [40] is a fundamental test case for the development of turbulence modeling and/or numerical techniques as it is the simplest realization of the turbulent flow. On the one hand, the capability and quality of LES part in DDES can be evaluated. On the other hand, the empirical parameter C_{DES} can be recalibrated. At the same time, the dissipation level of the present in-house CFD code can be evaluated. To obtain more resolved turbulence, the dissipation level of the numerical scheme should be reduced effectively wherever LES acts.

1. *Calibration of C_{DES} with Fourth-Order Central Scheme*

The computational domain contains 32^3 or 64^3 uniform cells. The computation of DIT is established in a cubic domain with periodic boundary conditions in all three directions to reflect the homogeneity of the flow.

The spatial scheme used in this calibration is the fourth-order central scheme without the conventional second-order artificial viscosity, but a very small fourth-order Jameson-type [41] artificial dissipation coefficient is introduced [where $k'(4) = 0.0001$] to suppress the spurious oscillations. The temporal scheme is the implicit LU-SGS method with very small nondimensional time stepping (0.0001 here).

Like Menter's SST model, the C_{DES} also contains k-ω and k-ε branches, which can be calibrated separately. Despite this the k-ε part is more important than the k-ω part for the DIT case. The final C_{DES} is coupled by the blending function F_1, i.e., $C_{\text{DES}} = F_1 \times C_{\text{DES},k\text{-}\omega} + (1 - F_1) \times C_{\text{DES},k\text{-}\varepsilon}$. The calibration procedure of SST-DDES is the same as that for SST-DES [23].

Figure 2 shows the energy spectra at $t = 0.87$ and 2.0, compared with the C_{DES} originally calibrated by Travin, where $C_{\text{DES},k\text{-}\omega} = 0.78$ and $C_{\text{DES},k\text{-}\varepsilon} = 0.61$. If C_{DES} is taken as the Travin's values, the present code underpredicts the energy cascade. But if C_{DES} is reduced in a manner $C_{\text{DES},k\text{-}\omega} = 0.4$ and $C_{\text{DES},k\text{-}\varepsilon} = 0.3$, the computational results agree the measurements very well. The difference of C_{DES} reflects the dissipation level of the different CFD code. In the following test cases, the C_{DES} is taken as the new value calibrated here. When $t = 2.0$, both branches of DDES can well predict the energy cascade, while the results of the k-ω branch look a little smaller than those of the k-ε branch. From the comparisons shown in Fig. 2, we can find that C_{DES} has a relatively small influence on the energy cascade.

At the same time, 64^3 cells are applied to predict the DIT with the same parameter as 32^3, also shown in Fig. 2. It is found that the dense grids can perform a bit better and resolve more turbulent energy spectra in a wider range of wave numbers as can be expected.

2. *Comparisons of Spatial Schemes*

As we know, it is often difficult to obtain the analytical and quantitative dissipation when a finite volume formulation is applied to calculate the complex turbulent flow. However, the effects of scheme dissipation on the turbulent energy spectra can be qualitatively explored through simulating DIT.

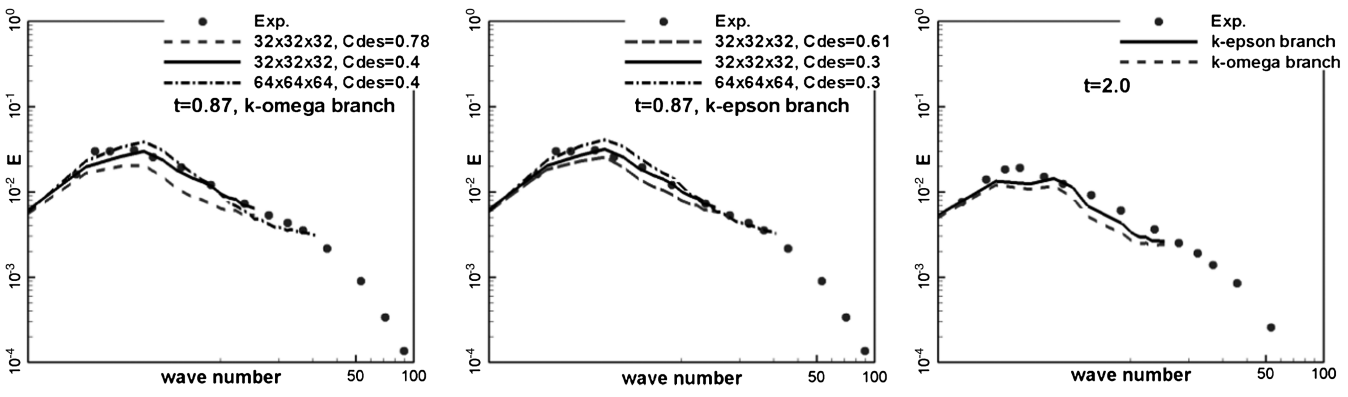

Fig. 2 Comparisons of energy spectra at $t = 0.87$ (left and middle: $C_{\text{DES}} = 0.4$ and 0.3) and $t = 2.0$ (right).

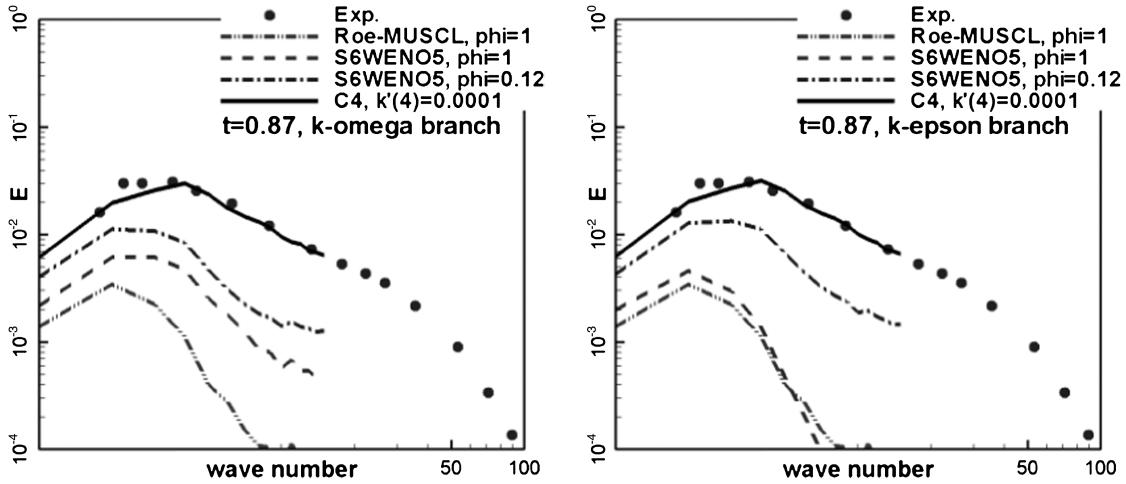

Fig. 3 Validation of the numerical schemes and the effect of the numerical dissipation in the SST RANS-LES turbulence modeling in decaying isotropic turbulence. The k-ω part (left) and the k-ε part (right).

Four schemes, such as original Roe scheme with the third MUSCL interpolation, two S6WENO5 schemes with full and 12% original dissipation, and the fourth central scheme only with fourth artificial viscosity where $k'(4)$ is equal to 0.0001, are investigated to explore the effect of the different numerical dissipation on the turbulent energy spectra. The last scheme can be approximately thought of as the S6WENO5 scheme with adaptive dissipation, where ϕ approaches zero in the LES region.

From the results shown in Fig. 3, original Roe scheme with the third MUSCL interpolation cannot well predict the energy cascade. Significant difference is demonstrated between the Roe scheme and measurements. It indicates that this kind of upwind scheme is too dissipative to predict the resolved turbulence. The S6WENO5 scheme with full dissipation also demonstrated significant dissipation as compared with the measurements despite its high-order symmetric scheme with relatively low dissipation through the fifth-order WENO interpolation. According to Bui [30], the scheme dissipation can be manually reduced through multiplying a small coefficient. Because the S6WENO5 scheme owns higher order than that of Bui, this value is not taken as 0.05 but 0.12. From the comparisons of turbulence energy cascade, the modified S6WENO5 scheme with 12% original dissipation reduces the gap between the computation and measurement as compared with the original S6WENO5 results. However, it still underpredicts the resolved turbulence energy. But it is nice to see that the high-order central scheme with an extremely small artificial dissipation satisfactorily predicts the turbulence energy spectra. It suggests that the S6WENO5 with adaptive dissipation, almost no dissipation in the separation region, can also well capture the DIT case.

As we know, the upwind scheme often underpredicts the turbulent energy spectra at high wave number. At low wave number, it can well predict the turbulence energy. However, from Fig. 3, the turbulent energy cascades using the three upwind schemes (original Roe, original S6WENO5, and S6WENO5 with only 12% dissipation) are much smaller than the measurements even at low wave number. The reason is as follows:

1) From Fig. 2, the grid density seems to have a relatively small influence on the energy cascade using the central scheme based on both 32^3 and 64^3 cells. Effects of the grid density using three upwind schemes, which are original Roe, original S6WENO5, and S6WENO5 with 12% dissipation, are presented in Fig. 4a. It can be found that the denser grids perform better. However, the original Roe scheme also cannot well predict the energy cascade, especially at high wave numbers even based on 64^3 cells. The original S6WENO5 scheme performs very similarly with original Roe scheme. Of course, original S6WENO5 performs a little better than original Roe scheme due to its higher order reconstruction. Fortunately, S6WENO5 with 12% dissipation can well predict the energy cascade at both low and high wave numbers based on 64^3 cells. It could be deduced that original Roe and S6WENO5 schemes can also perform better if the grids become dense sufficient, which leads to the significant reduction of computation efficiency. The S6WENO5 scheme with 12% dissipation can predict the separation very well based on appropriate grid density with relatively high computation efficiency.

2) As mentioned before, our in-house code is a compressible solver and both limiter and entropy fix are introduced to simulate the compressibility. Here, original Roe scheme with MUSCL interpolation is selected to explore the effects of limiter in Eq. (9) and Radespiel and Swanson entropy fix on the turbulent energy spectra. In Fig. 4b, the effects of limiter and Radespiel and Swanson entropy fix are presented. The original Roe scheme with both limiter and Radespiel and Swanson entropy fix obviously underpredicts at both low and high wave numbers. If the limiter is turned off, we find that the scheme without a limiter can well predict the turbulent energy spectra at low wave numbers and it underpredicts the energy cascade at high wave number. It even performs better than the original Roe scheme based on 64^3 cells. If the limiter and Radespiel and Swanson entropy fix are both turned off, the scheme also well predicts the energy cascade at low wave numbers and performs much better than the scheme without a limiter and the original Roe scheme at high wave numbers, although it still underpredicts the energy cascade at high wave numbers. Thus, if the original Roe scheme is hoped to predict the massive separation flow, the limiter and entropy fix should be turned off, the dissipation should be effectively reduced, and the grid density also should be large enough.

From the preceding comparisons, the numerical dissipation, grid scale, limiter, and entropy fix of the spatial scheme have a significant influence on the energy cascade, while the parameter C_{DES} has a relatively weak influence.

B. Tandem Cylinders

Flow around TC is a good test case for numerical and turbulence simulation. The flow is known to associate with complex flow phenomena like the transition on the two cylinders, separation of turbulent boundary layer, free shear layer instability, the interaction of unsteady wake of the front cylinder with the downstream one and unsteady massively separated flow between the cylinders and in the wake of the rear cylinder, and so on. The capability of turbulence models developed and the spatial and temporal methods adapted in the numerical simulation procedures can thus be fully explored in terms of the quality of reproducing the complex physics related to the flow.

The TC case studied here is the one investigated experimentally by Jenkins et al. [4,5] and Neuhart et al. [6], which is a standard test case in the ATAAC project [7] and BANC workshop [8,9]. The diameters of the two cylinders are the same. The spacing L is $3.7D$. The mesh in

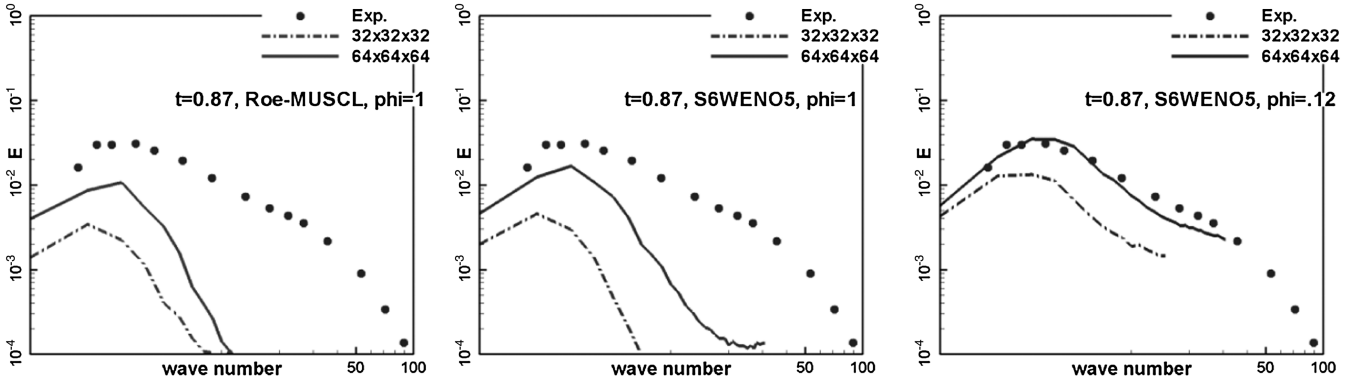

a) Grid density effects for the upwind schemes

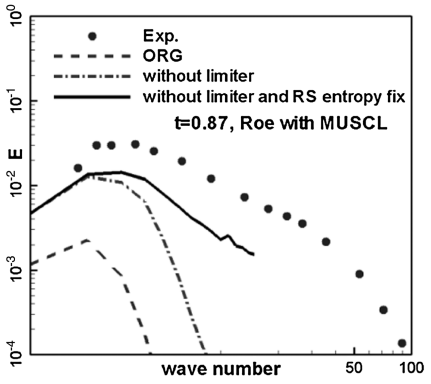

b) Limiter and R-S entropy fix effects in original Roe scheme (32^3)

Fig. 4 Performance of upwind schemes (k-ε part).

this paper is the mandatory mesh in ATAAC, generated by New Technologies and Services. The total cells in the $x-y$ plane are about 82,000. To predict the small scale structures, the two-dimensional grids between the cylinders are almost isotropic (about $0.01 \sim 0.02D$). The spanwise domain is taken as three-dimensional with equal intervals of $\Delta z = 0.02D$. The overall cells are 12.4×10^6 for the three-dimensional domain. In this paper, almost all the computations are based on the mandatory grids except the investigation on the effects of grid density and spanwise computation domain.

The velocity of freestream is 44 m/s, the Reynolds number based on D is 1.66×10^5, and the angle of attack is 0 deg. The non-dimensional time step is 0.01. To obtain high temporal order, about 80 subiterations are applied to converge in a physical time step.

In the present simulations, no-slip conditions were imposed on the cylinders' walls. Symmetric conditions were applied on the lateral sides of the wind-tunnel test section; periodic conditions were taken in the spanwise direction. At inflow and outflow boundaries, the one-dimensional Riemann characteristic analysis was employed to construct a nonreflection boundary condition. "Ghost cells" are employed to treat all kinds of boundary conditions including the boundaries of the adjacent zonal domains.

In the following figures it is noted here that the filled triangle symbol (▲) denotes the measurement data when the rear cylinder has

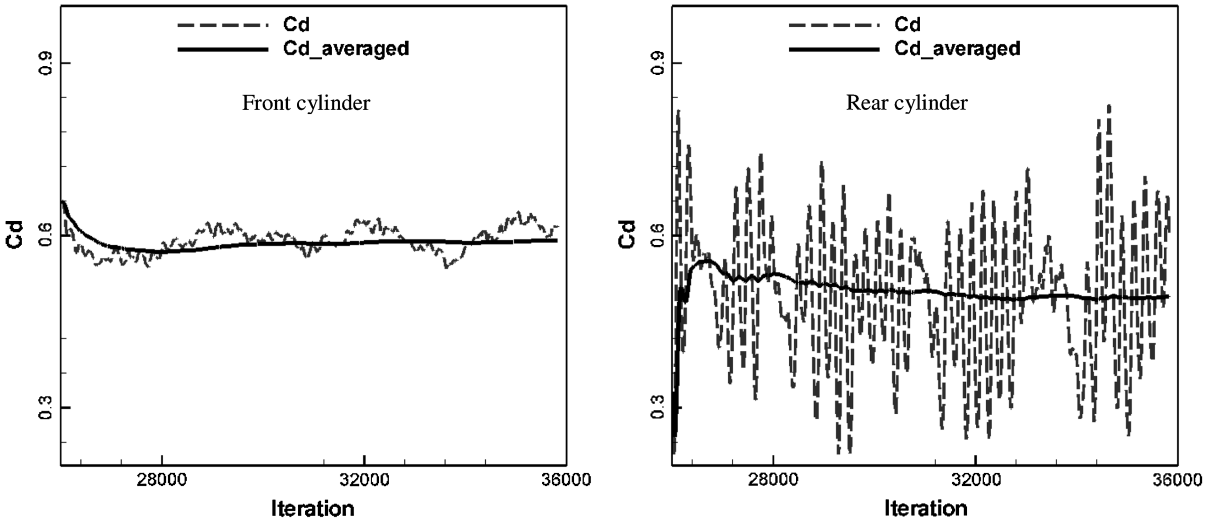

Fig. 5 History of instantaneous and time-averaged C_d of the front and rear cylinders.

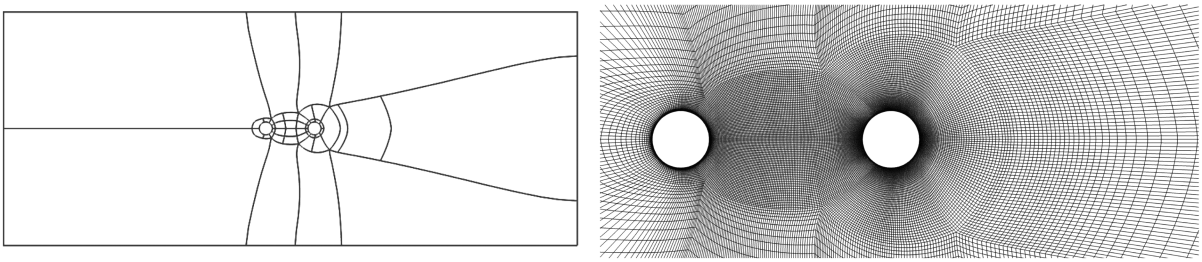

Fig. 6 Coarse grids past TC (left: grid topology; right: near-field grids).

no fixed trip (Exp.1 for short); the filled circle dot (●) is for the measurement data when the rear cylinder has a fixed trip (Exp.2 for short).

1. Histories of Drag Coefficients

Figure 5 presents the histories of the drag coefficient (C_d) on the front and rear cylinders by S6WENO5 with adaptive-ϕ, where ϕ is defined in Eq. (2) and it ranges from 0 to 1. The grids are the mandatory grids. From the mean C_d, we can find that the C_d of the front cylinder (0.59) is larger than that of the rear one (0.49). However, the C_d fluctuation amplitude of the front cylinder is significantly smaller than that of the rear one. The flow past the front cylinder seems relatively "quiet." This feature is easily understood as the front cylinder encounters weaker upstream disturbances than the rear one, which is in the extremely unsteady wake detached from the front cylinder.

2. Effects of Grid Scale

To explore the effects of grid scale, coarse grids are generated with almost the same topology of the mandatory grids, shown in Fig. 6. The coarse grids are about 70% grid points in all three directions compared with the mandatory grid required in ATAAC. That is, in the $x-y$ plane shown in Fig. 6, the grid number is about 43,000. The spanwise domain is taken as three-dimensional with equal intervals of $0.03D$. Thus, the total grid number is about 4.3×10^6 with the same domain as for the mandatory grid. The S6WENO5 scheme with adaptive dissipation is taken as the spatial scheme.

In this subsection, we briefly demonstrate the effects of grid density on the mean pressure and velocity, pressure fluctuation, and instantaneous flow structures, shown in Fig. 7. The detailed analysis of flow features will be presented in Sec. V.B.4.

From the comparisons of the mean pressure coefficients, both grids can well match the measurements, while the coarse grid underpredicts the pressure recovery slightly (Fig. 7a). From the comparisons of the streamwise velocity in the gap region between the two cylinders and in the wake after the rear cylinder (Fig. 7b), the coarse grid results severely underpredict the recirculation behind the front cylinder but give overprediction for the rear cylinder. The coarse grids underpredict $C_{p,\mathrm{rms}}$ due to relatively larger grid size (Fig. 7c). Although the coarse grids can exhibit the small scale structures, the scales of structures look larger than those of dense grids through the comparisons of the instantaneous spanwise vorticity and Q criterion (Figs. 7d and 7e). At the same time, the small scale structures of the coarse grids look less than those of dense grids.

Then, the computations in the following sections are all based on the dense grids in the x-y plane.

3. Effects of Spanwise Length

When the periodic condition is applied, the spanwise length is one of the important parameters. In this subsection, two spanwise lengths, one diameter and three diameters with the mandatory two-dimensional grids, are applied to investigate the effects of spanwise length on the mean pressure, velocity, pressure fluctuations, and instantaneous flow structures. For the one-dimensional case, 51 points are used in the spanwise direction. The spatial scheme is S6WENO5 with adaptive dissipation.

From the comparisons of the mean pressure coefficients, the results of these two grids can well match the measurements. However, from the comparisons of the streamwise velocity in the gap region between the two cylinders and in the wake after the rear cylinder (Fig. 8b), the one-diameter case severely underpredicts the recirculation behind the front cylinder but gives severe overprediction for the rear cylinder. The one-diameter case also underpredict $C_{p,\mathrm{rms}}$ due to relatively small spanwise length (Fig. 8c). Because of the same two-dimensional grids in the x-y plane, the instantaneous spanwise vorticities in the one- and three-diameter cases look similar (Figs. 7d and 7e). The computations in the following sections are thus all based on the mandatory mesh with three-diameter spanwise length.

4. Effects of Numerical Dissipation of the Spatial Scheme

In this subsection, three spatial schemes, the original Roe scheme with the third MUSCL interpolation and two S6WENO5 schemes with two low-dissipation approaches (parameter ϕ is taken as a constant and an adaptive function, respectively), are employed in the computation in exploring the capabilities of these schemes and the effects of numerical dissipation on turbulence simulations.

In this subsection, if there are no special notes, the solid line indicates the results of the S6WENO5 scheme with adaptive ϕ (shortened as A-ϕ), the dash-dotted line indicates those for the S6WENO5 scheme with constant ϕ (C-ϕ for short, where $\phi = 0.12$), and the dashed line indicates those for the original Roe scheme with MUSCL interpolation including limiter and entropy fix (original Roe scheme for short). The contours have the same levels labeled in the same type of figures.

In addition, all the computations are based on the mandatory grids with three-diameter spanwise length.

a. Mean Flow. The mean flowfields, such as pressure coefficient on both cylinders, velocity, and spanwise vorticity around TC are presented as detailed as possible. The time-averaging procedure is from step 26,000 to step 36,000. This range ensures enough samples for statistics.

First, the mean pressure coefficients are shown in Fig. 9. On the front cylinder, fixed trip was applied in both experiments. The negative peak of C_p of original Roe scheme is much larger and the separation point occurs more downstream than the measurements and the other two computations. The fixed trip on the rear cylinder in experiments results in the difference of C_p. If no trip is applied, the negative peak of the pressure coefficients is larger, about 0.3. In the fully separated region, the computational pressure coefficients show a slight difference. The results by C-ϕ and A-ϕ do not present significant difference in the pressure distribution on both cylinders.

The comparisons on the streamwise velocity along the two centers among the three computations and two measurements are presented in Fig. 10. The reattachment points in the gap and after the rear cylinder are presented in Table 1. The scheme dissipation has a distinct effect on the streamwise velocity. The performance of the A-ϕ approach is the best.

In the gap region, the large dissipation original Roe scheme suppresses the flow separation behind the front cylinder and the recirculation is much smaller than that of measurements. The low-dissipation schemes predicted the streamwise velocity development along the centerline better although the recirculation is somewhat

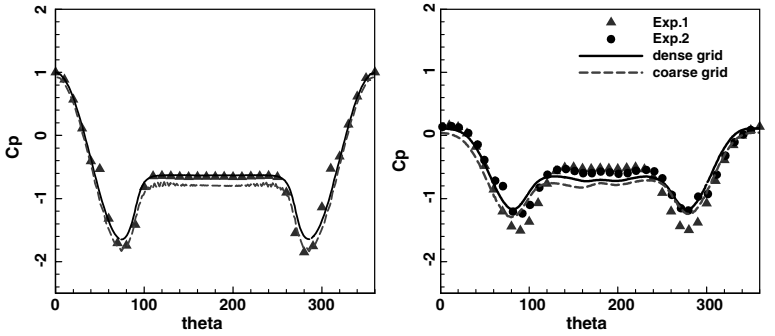

a) Mean pressure coefficients on the tandem cylinder surfaces (Left: front; Right: rear)

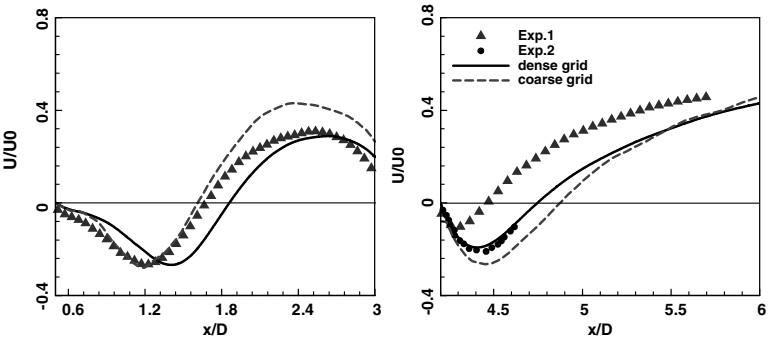

b) Mean streamwise velocity at the centerline between the cylinders (left) and after the rear cylinder (right)

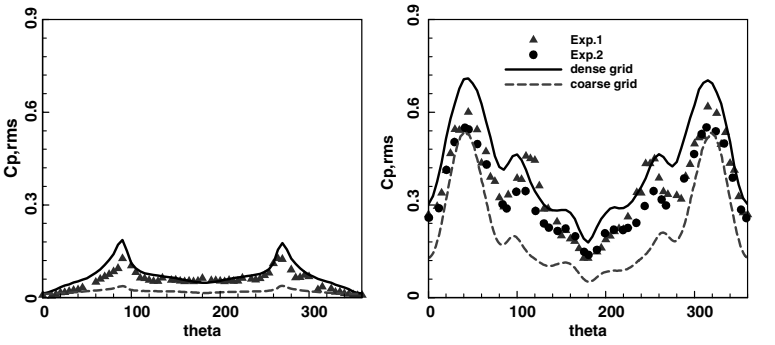

c) RMS pressure coefficients on the tandem cylinder surface (Left: front; Right: rear)

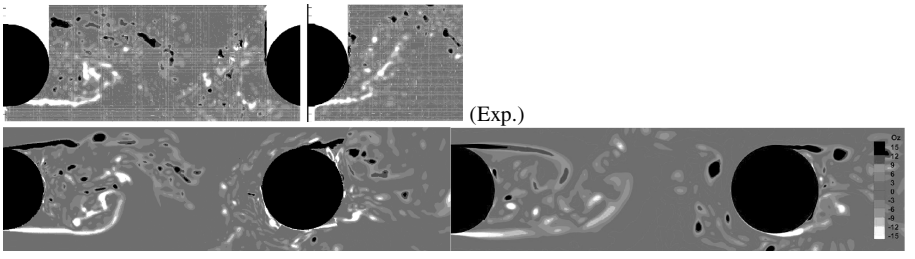

d) Instantaneous spanwise vortices (Left: dense grids; Right: coarse grids)

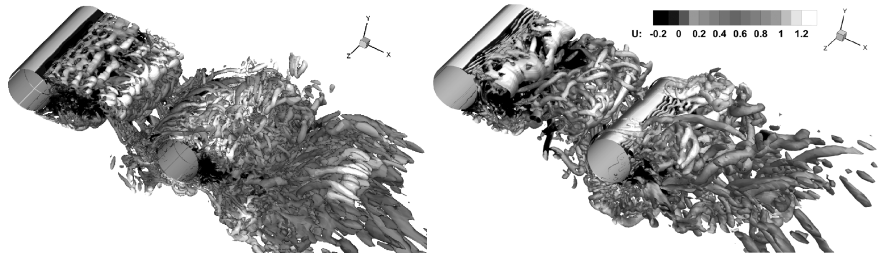

e) Instantaneous Q criterion (Left: dense grids; Right: coarse grids)

Fig. 7 Effects of the grid density on the quality of the numerical results.

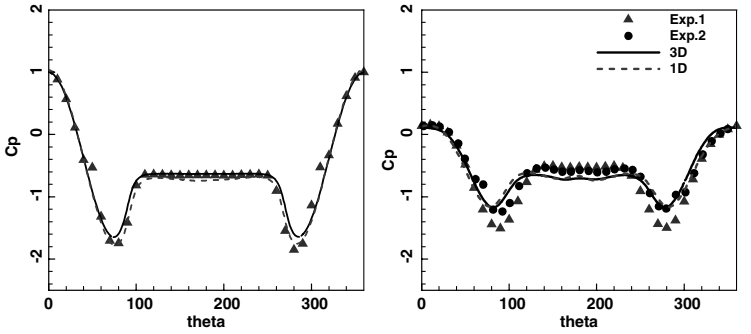

a) Mean pressure coefficients on the tandem cylinder surfaces (Left: front; Right: rear)

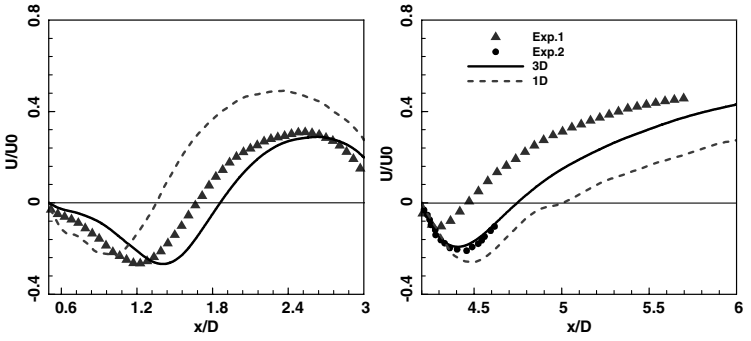

b) Mean streamwise velocity at the centerline between the cylinders (left) and after the rear cylinder (right)

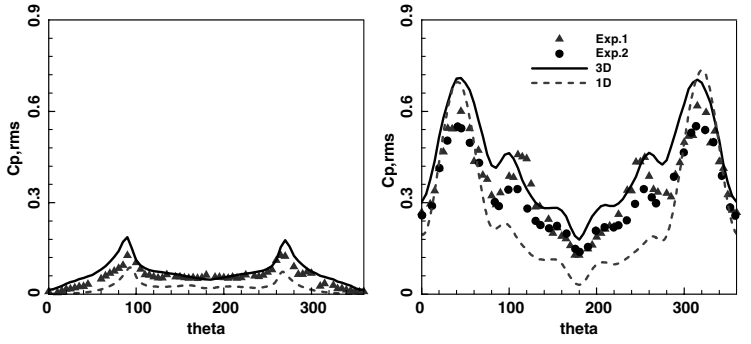

c) RMS pressure coefficients on the tandem cylinder surfaces (Left: front; Right: rear)

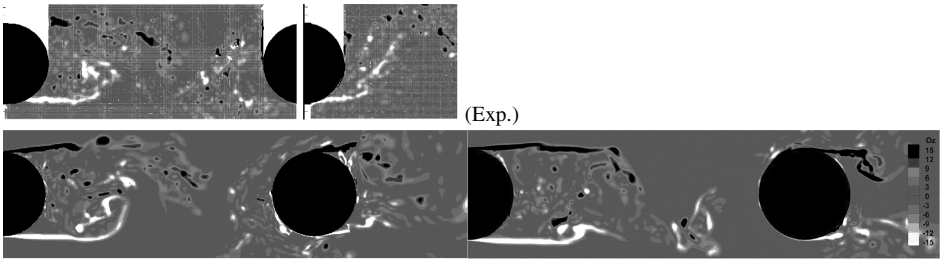

d) Instantaneous spanwise vortices from 3D (left) and 1D (right) spanwise domains.

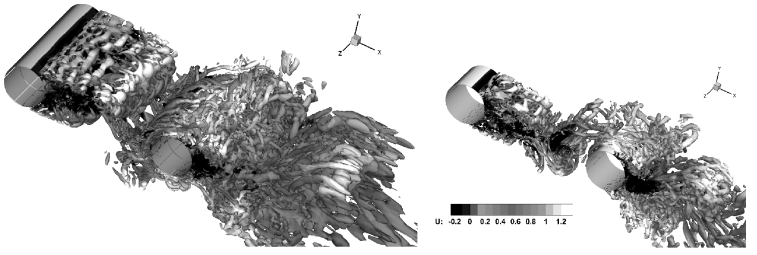

e) Instantaneous Q criterion from 3D (left) and 1D (right) spanwise domains

Fig. 8 Effects of spanwise domain size on the computational results.

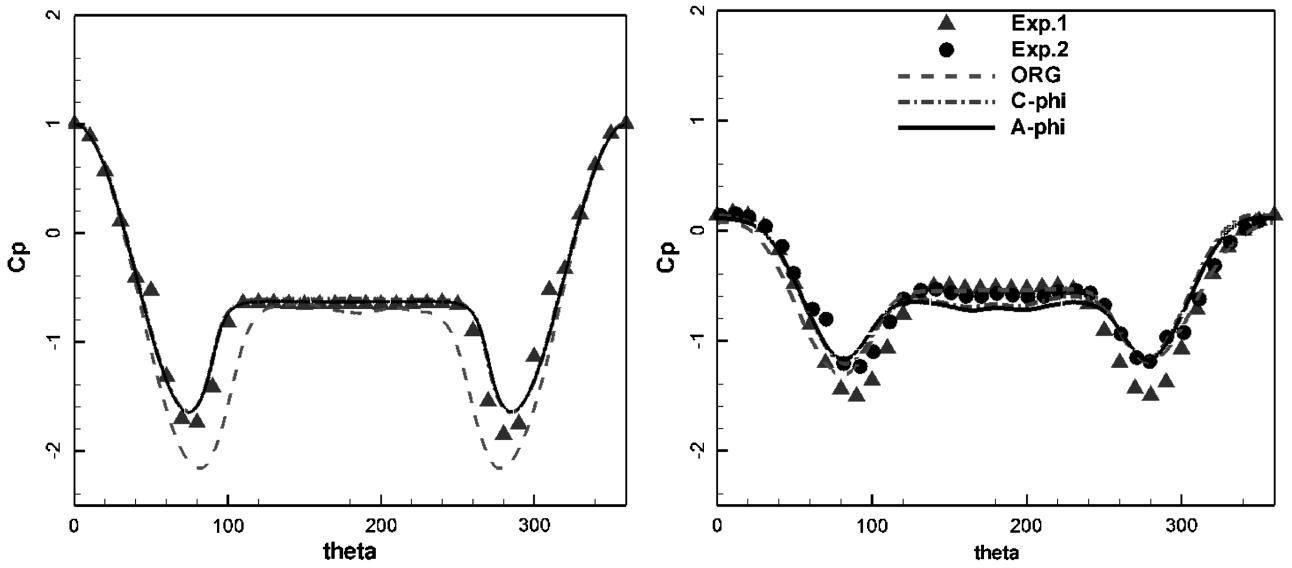

Fig. 9 Mean pressure coefficients on the TC surfaces (left: front; right: rear).

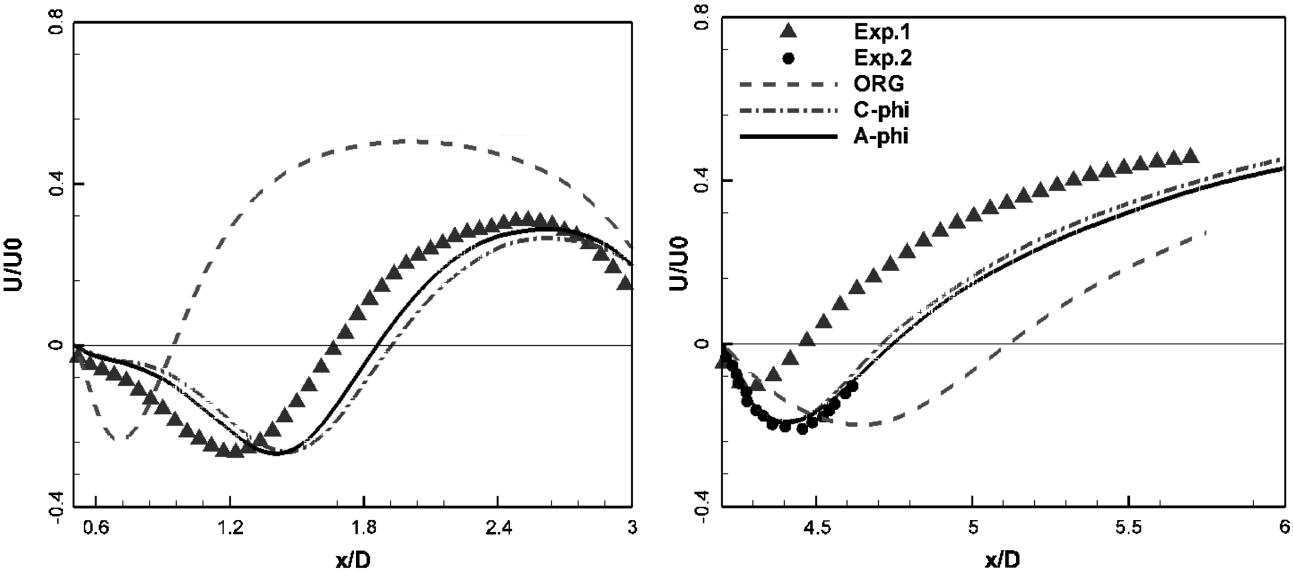

Fig. 10 Mean streamwise velocities at the centerline between the cylinders (left) and after the rear cylinder (right).

Table 1 Streamwise coordinates of the reattachment points along the central line

Region	Exp. 1	Exp. 2	Original Roe scheme	*C*-ϕ	*A*-ϕ
Gap	1.67	——	1.00	1.93	1.85
Wake after rear cylinder	4.46	——	5.12	4.71	4.74

larger than the measurement. The reason can be attributed to the fact that the fixed trip in the experiment triggered stronger transition to turbulence than what is resolved in the present numerical simulation. The difference between the *A*-ϕ and *C*-ϕ approaches is small but the former scheme appears slightly more satisfactory than the latter one.

In the wake behind the rear cylinder, the fixed-transition trip has an obvious effect on the recirculation, which is corresponding to those of C_p (already shown in Fig. 9) and $C_{p,\mathrm{rms}}$ (shown in a later figure). However, the reason why the recirculation without the fixed trip is

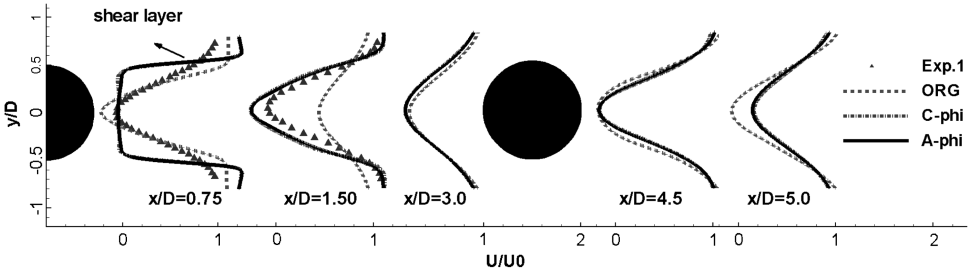

Fig. 11 Mean velocity profiles at several streamwise locations.

much smaller than that with the fixed trip is not clear. It should be deeply investigated in the future. It is encouraging that the low-dissipation scheme provides the velocity distribution similar to the measurement data with fixed trips. The recirculation by A-ϕ looks a little larger than that of C-ϕ.

The velocity profiles at several streamwise locations can reflect the loss and recovery of the flow in the gap between the two cylinders and in the wake behind the rear cylinder, shown in Fig. 11.

Corresponding to a relatively larger recirculation behind the front cylinder by the low-dissipation schemes, the loss in velocity looks also larger than that of the measurement before the reattachment point between the cylinders. At the location of $x/D = 0.75$, the shear layer by the low-dissipation scheme is obviously much sharper than the measurements. The possible reason is the insufficient growth of resolved turbulence. Because of very small recirculation behind the front cylinder by the original Roe scheme, the flow recovers much faster than those of the low-dissipation schemes and the measurement. After the reattachment point, small differences occur for all the three schemes.

In the wake of the rear cylinder, due to much larger recirculation by original Roe scheme, the loss in velocity appears larger than those in the low-dissipation schemes.

The comparisons of time- and spanwise-averaged streamwise velocity contours are presented in Fig. 12, together with the modeled eddy viscosities. The low-dissipation C- and A-ϕ schemes agree with the velocity distribution well with the measurement and little difference exists. However, the modeled eddy viscosities by these two schemes demonstrate significant difference. The eddy viscosity by the A-ϕ scheme is much smaller than by the C-ϕ scheme after the rear cylinder. The original Roe scheme, however, shows distinct difference on velocity distribution from those of the measurements. Much smaller recirculation in the gap region and much larger recirculation in the wake after the rear cylinder are demonstrated. The modeled eddy viscosity by original Roe scheme in the wake of the front cylinder also looks much larger than those of the low-dissipation schemes. Then, DDES with the most dissipative original Roe scheme performs like the URANS with very large modeled eddy viscosity.

Figure 13 presents the contours of the time- and spanwise-averaged spanwise vorticity, which can easily reflect the feature of the shear layer. In the gap region, the shear layer by the original Roe scheme is much shorter than that of measurements and the other two computations. However, in the wake after the rear cylinder, the shear layer is a little longer than that of experiments, which means larger recirculation. The shear layers by the two low-dissipation schemes well match the measurement and show little difference, despite that the shear layer by A-ϕ is a little shorter than that of C-ϕ. In fact, the computational shear layers by A- and C-ϕ schemes are a little narrower than that of measurements.

b. Instantaneous Flow. The comparisons of instantaneous spanwise vorticity are presented in Fig. 14. From the measurements, very small scale structures are observed in the gap region and in the

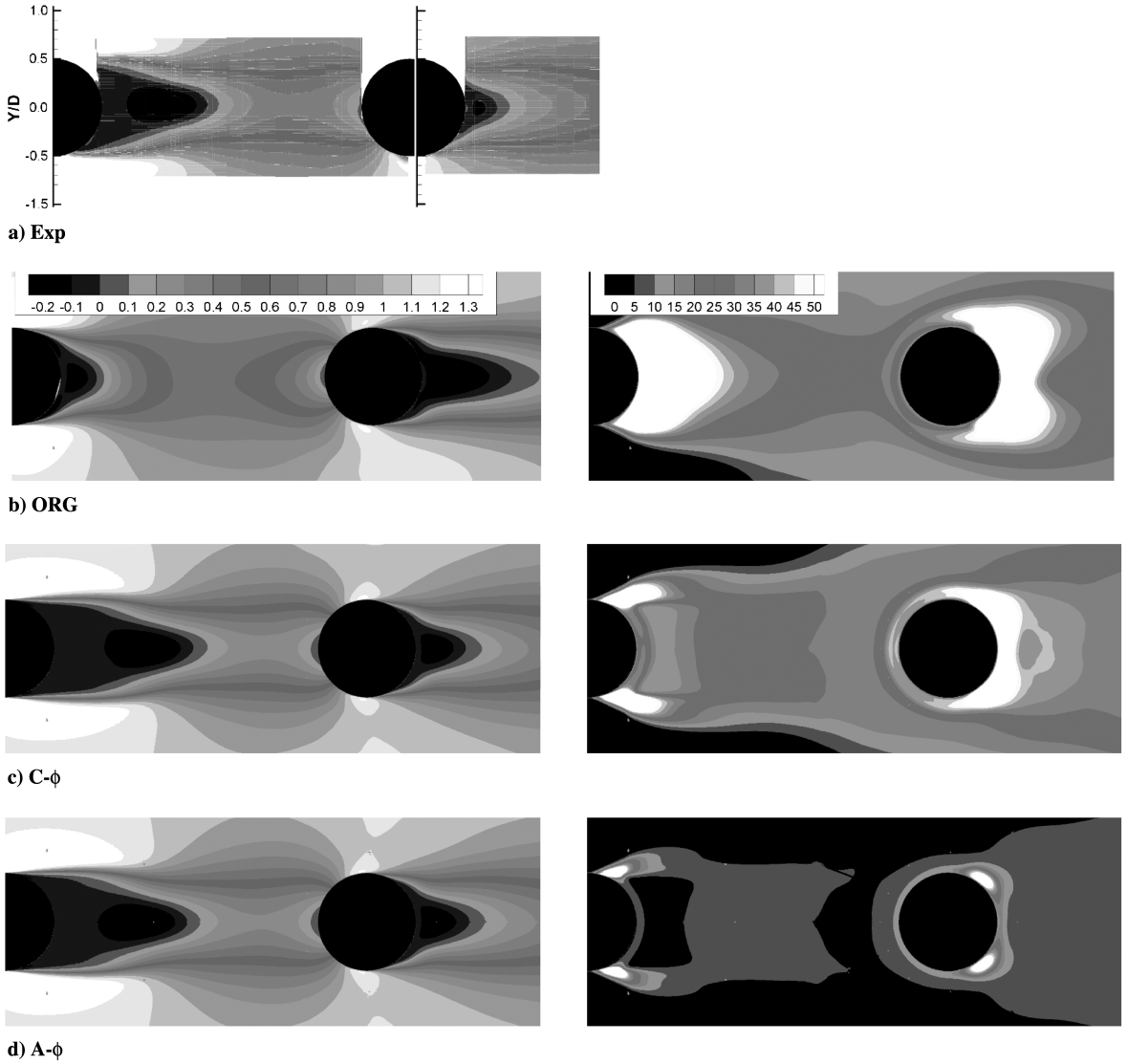

Fig. 12 Time-and spanwise-averaged streamwise velocity contours (left column) and modeled eddy viscosity (right column).

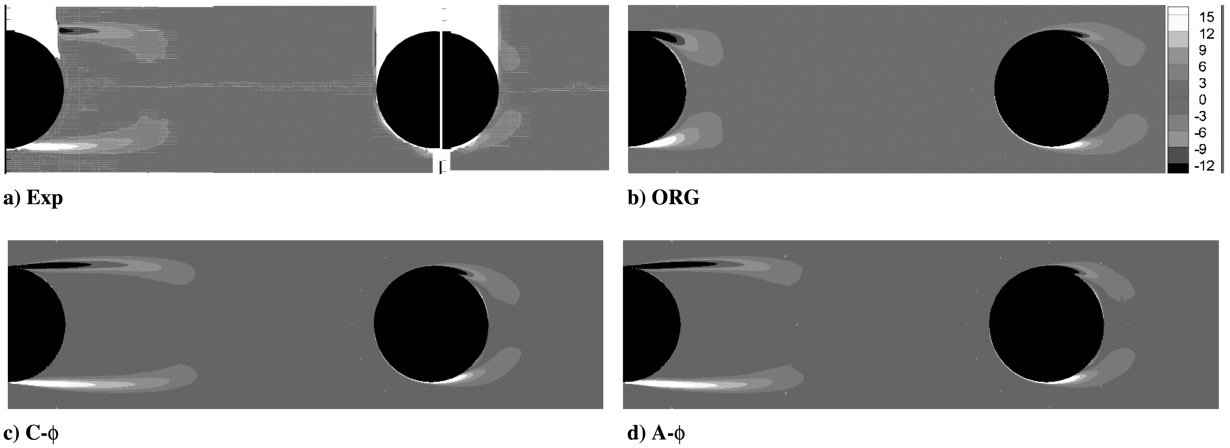

Fig. 13 Comparison of the mean spanwise vorticity contours from different dissipation approaches with the experiment.

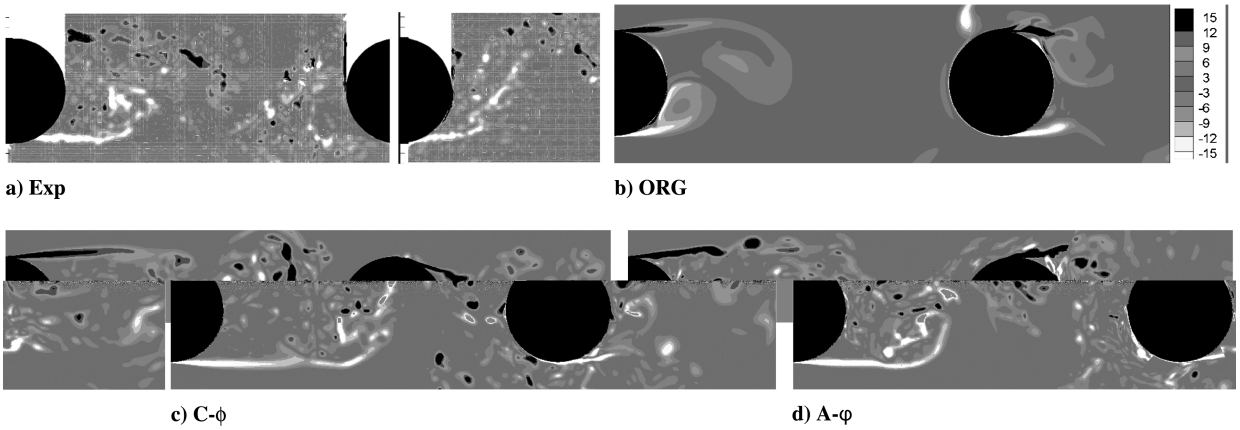

Fig. 14 Comparison of the instantaneous spanwise vorticity contours from different dissipation approaches with the experiment.

wake after the rear cylinder. Because of its large dissipation, the original Roe scheme only presents very large structures, just like Kármán vortex shedding. Almost no small structures are resolved and demonstrated by the original Roe scheme. Both *A*- and *C*-ϕ schemes can capture the small scale structures similar to the measurement. However, the numerical shear layers appear a little longer than that of the measurement. The *C*-ϕ results demonstrate a little longer shear layer and a slightly larger coherent structure than those of the *A*-ϕ. It indicates that the shear layer instability by *C*-ϕ takes place later than that of the measurement and *A*-ϕ. After the rear cylinder, more structures are observed by *A*-ϕ than *C*-ϕ. This phenomenon can also be observed from Fig. 15.

In Fig. 15, we can also find that the scales of coherent structures by *A*- and *C*-ϕ schemes are much smaller than those of the original Roe scheme although all these results are on the same grids and SST-DDES. The performances of *C*- and *A*-ϕ schemes appear similar and both of them can capture the small scale turbulent structures between the two cylinders and in the wake after the rear cylinder. The distinguishable difference between the *C*- and *A*-ϕ results can be observed in the shear layer region after the front cylinder. Relatively smaller scale structures and more obvious shear layer instability by the *A*-ϕ scheme can be found than those by the *C*-ϕ scheme. The *C*-ϕ approach cannot demonstrate the detailed fine-scale structures in the shear layer because its dissipation is manually decreased without any

Table 2 Primary frequency predicted by different schemes

DDES	Primary frequency at sample A, Hz	PSD at sample A, dB	Primary frequency at sample B, Hz	PSD at sample B, dB
Original Roe scheme	197	131	197	136
C-ϕ	169	111	169	135
A-ϕ	169	117	169	138
Experiment	181	118	181	139

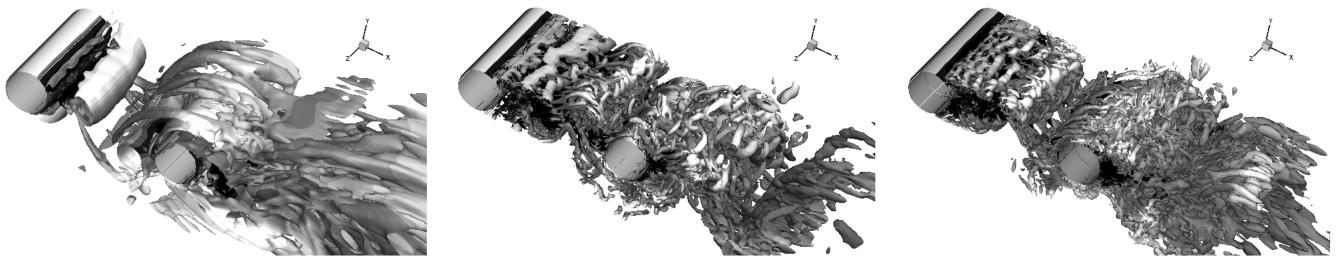

Fig. 15 Illustration of the Q criteria around TC with three dissipation approaches.

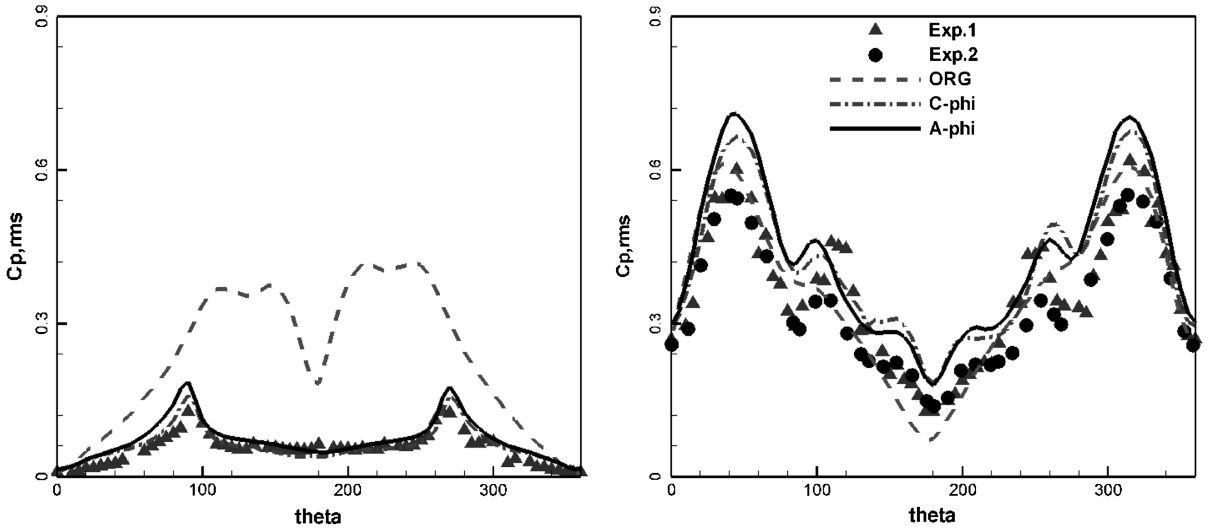

Fig. 16 The RMS of pressure coefficient on the TC surfaces (left: front; right: rear).

physical mechanism. Therefore, the dissipation has a significant effect on the flow structures in the shear layer behind the front cylinder. In the wake after the rear cylinder, the scale of structures by the A-ϕ scheme is also a little smaller than that by the C-ϕ scheme. The original Roe scheme cannot well simulate the small scale of structures. Only two-dimensional large-scale structures in the gap region and few three-dimensional large-scale structures in the wake behind the rear cylinder are observed.

c. Pressure Fluctuation. The RMS fluctuating pressure coefficients ($C_{p,\mathrm{rms}} = P_{\mathrm{rms}}/(0.5\rho U_0^2)$) can reflect the magnitude of the pressure fluctuation on the cylinder surface. The coefficients of $C_{p,\mathrm{rms}}$ on the two cylinders are shown in Fig. 16.

On the front cylinder surface, similar with the distribution of C_p, low-dissipative C- and A-ϕ schemes perform better than that of the original Roe scheme. The original Roe scheme is more dissipative with very strong two-dimensional Kármán vortex shedding; the

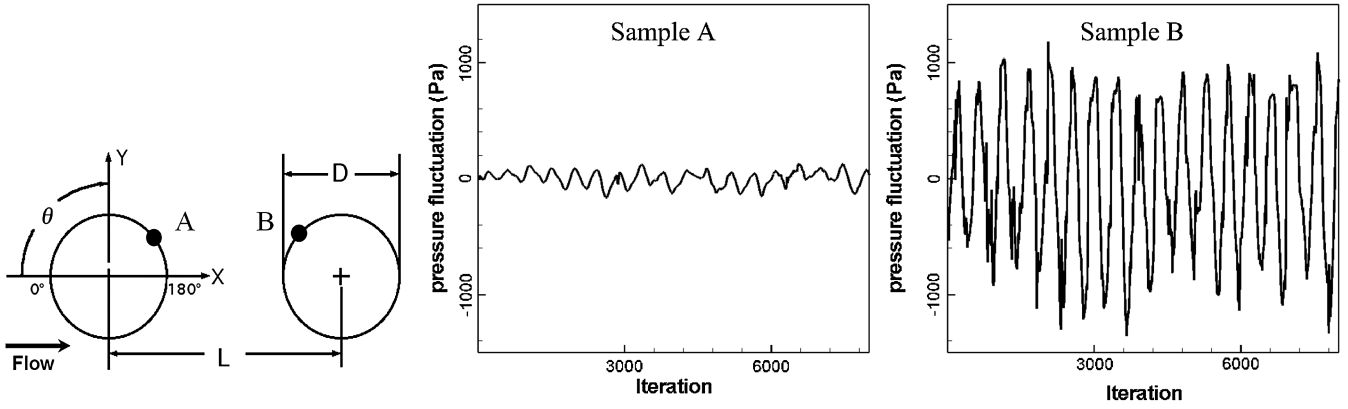

a) History of pressure at Sample A and B

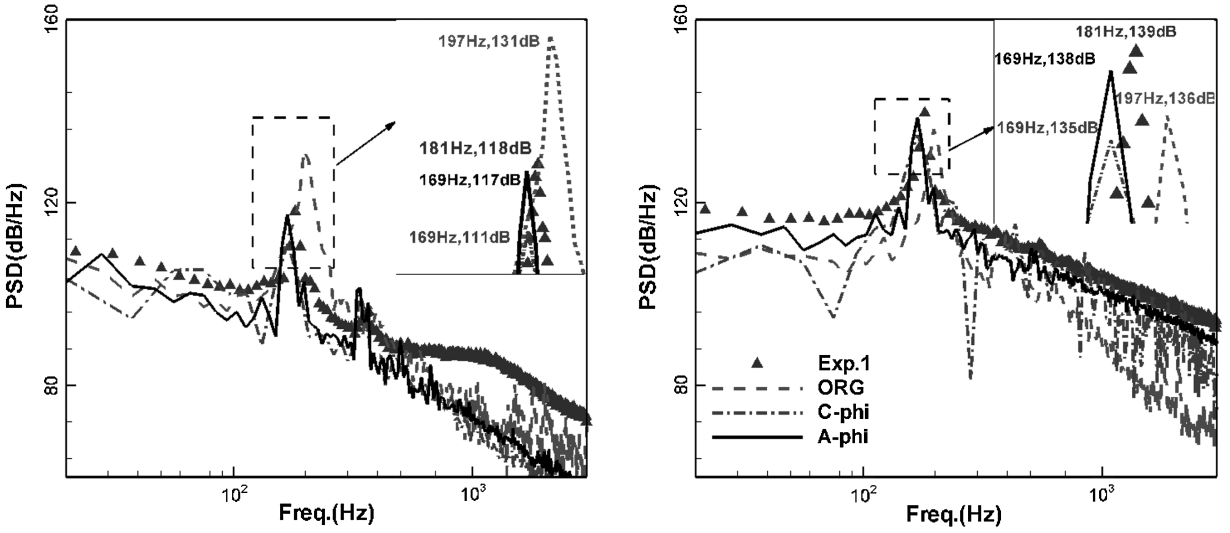

b) PSD of Sample A **c) PSD of Sample B**

Fig. 17 History of the pressure and PSD at locations A and B.

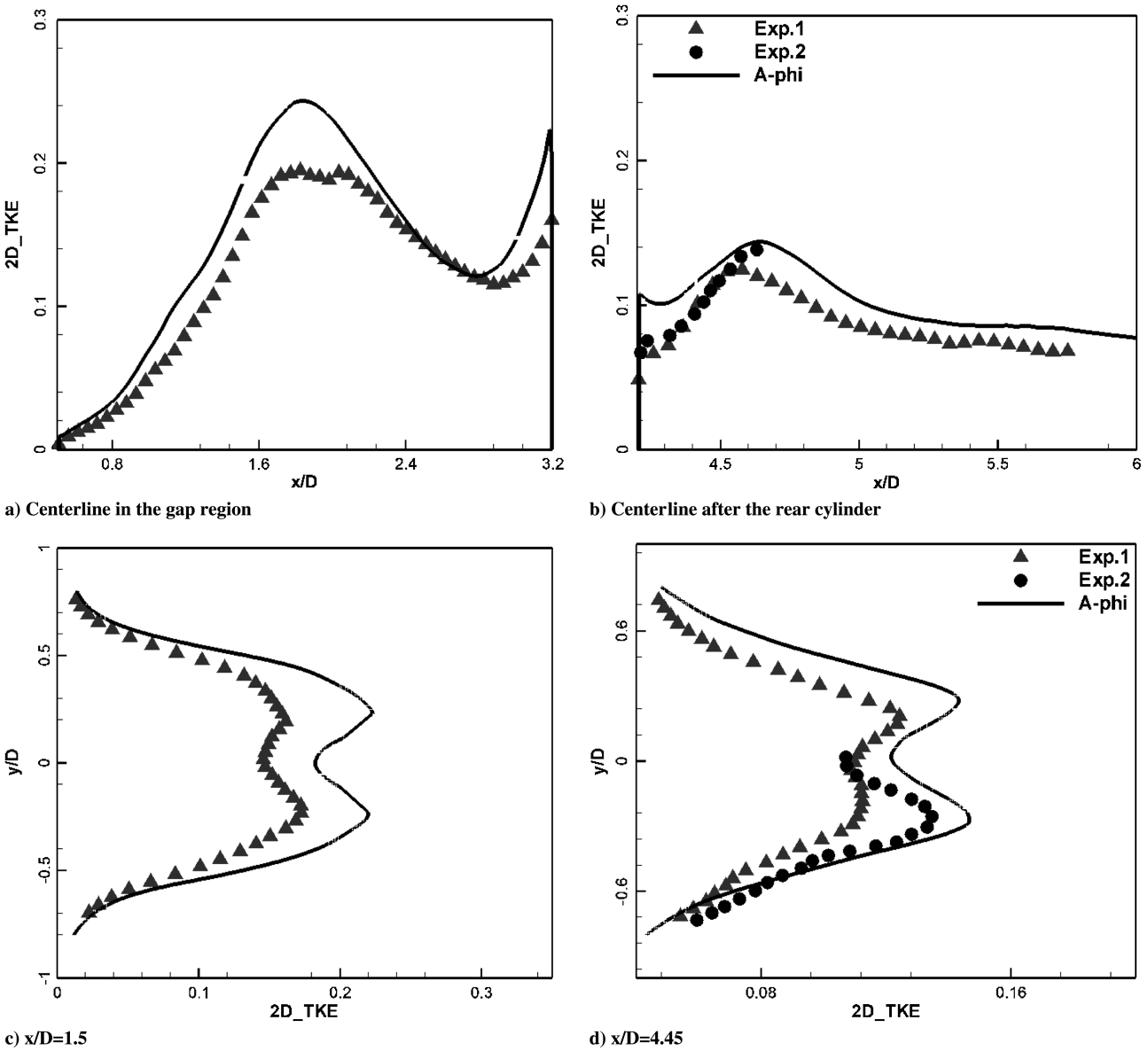

a) Centerline in the gap region

b) Centerline after the rear cylinder

c) x/D=1.5

d) x/D=4.45

Fig. 18 Comparisons of TKE at the centerline and two streamwise locations.

pressure fluctuation looks more obvious, leading to much larger $C_{p,\mathrm{rms}}$ than those of measurements and the two computations. Because of fully turbulent hypothesis, the values of $C_{p,\mathrm{rms}}$ with high-order schemes with low dissipation are a little larger than those of the measurements in the windward side. Near 90 and 270 deg, the separations from the surface lead to a relatively larger $C_{p,\mathrm{rms}}$.

On the rear cylinder surface, both *C*- and *A*-ϕ schemes can well capture the primary peak of $C_{p,\mathrm{rms}}$ at 45 deg, which is induced by the vortex shedding from the front cylinder and the secondary peak from 110 to 120 deg. The original Roe scheme almost cannot present any secondary peak in $C_{p,\mathrm{rms}}$. The trips on this cylinder lead to a smaller and more upstream secondary peak of $C_{p,\mathrm{rms}}$.

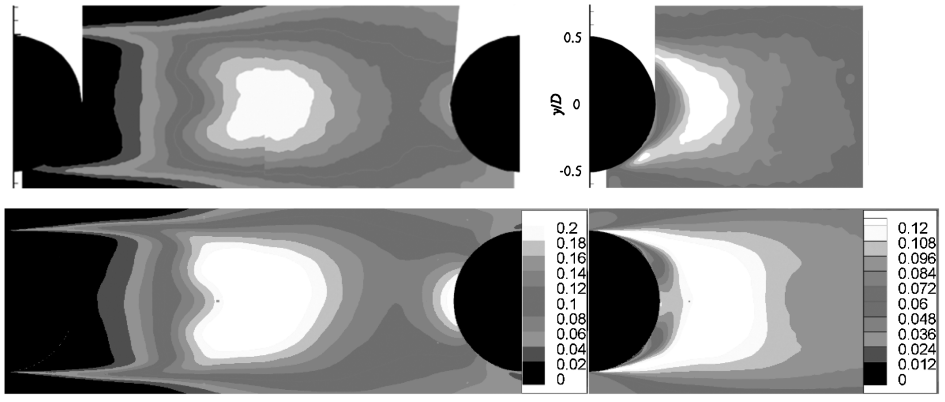

Fig. 19 Mean TKE (top: exp; bottom: *A*-ϕ).

Because the flow is typically unsteady and strongly turbulent, the history of pressure fluctuation provides power spectral density (PSD) information illustrated at two samples, one is 135 deg on the front cylinder (sample A) and the other is 45 deg on the rear cylinder (sample B), shown in Fig. 17. The primary vortex shedding frequency and corresponding magnitudes are listed in Table 2.

The frequency of the fluctuating pressure at sample A is the same as that of sample B. However, different schemes deliver different frequencies. The frequencies of both *A*- and *C*-ϕ schemes are 169 Hz, while the frequency of original Roe scheme is 197 Hz. In fact, the frequency of the measurement data is 181 Hz.

The magnitude of the pressure fluctuation reflects the dissipation level of schemes. On the front cylinder surface, original Roe scheme presents much larger PSD, about 13 dB, than that in the measurement. The *A*-ϕ approach provides the best performance in PSD among the three schemes with only 1 dB smaller than that of the measurement. On the rear cylinder surface, three schemes predict the similar PSD and only 1–3 dB smaller than that of the measurement. The main reason can be attributed to the smaller scales of turbulence near the rear cylinder.

From the comparisons of PSD at sample A and B on both cylinder surfaces, the maximum noises are generated from the windward side of the rear cylinder surface, which can reflect the periodical impingement of the vortex shedding from the front cylinder.

5. *Turbulence Flowfields Using A-ϕ Scheme*

For the distribution of TKE, only the *A*-ϕ scheme is applied due to its better performance. The two-dimensional TKE is defined as $\text{TKE} = (\overline{u'u'} + \overline{v'v'})/2U_o^2$, where we ignore the spanwise components due to the periodic condition. Some TKE profiles, such as along the central line and at two streamwise locations, are plotted in Fig. 18 and TKE contours are plotted in Fig. 19.

In the gap region, the computational TKE is slightly more overpredicted than the measurements. In the wake region behind the rear cylinder, the TKE is again slightly overpredicted along the central line but the peak agrees well with the tripped experimental data. Because of a slightly larger and a little more downstream recirculation, the TKEs at the two streamwise locations appear also somewhat larger than those in the measurements. In fact, the present computational results are similar to the measurements with the fixed trip on the rear cylinder surface.

From the contours of TKE shown in Fig. 19, the computation overpredicts the TKE and the maximum of TKE locates slightly further downstream than the measurements.

6. *Instantaneous Flow Structures in a Period*

Several instantaneous spanwise vorticities and the isosurfaces of λ_2 in a period are presented in Fig. 20. We can see the shear layer growth, instability, vortex shedding, vortex interaction, vortex impingement on the rear cylinder, and vortex shedding again from the rear cylinder. These figures correspond to the points shown on the lift curve of the front cylinder indicating the flow behavior at the seven phases. Vortex shedding from the upper and lower surfaces of the front and rear cylinders alternates but the time-averaged flowfields are symmetric about the $y/D = 0$ central line and the time-averaged C_L is zero. From the lift coefficients of the cylinders, the front one is not synchronous with the rear cylinder.

The seven points or phases shown in Fig. 20a correspond to seven particular flow states as viewed from the lift curves for both the front and rear cylinders. Phase 1 and phase 7 indicate that the lift coefficient of the front cylinder is at minimum (or negative maximum); phase 2 corresponds to the minimum lift coefficient for the rear cylinder; phase 3 and phase 6 correspond to the zero lift of the front cylinder; and phase 4 and phase 5 correspond to the maximum lift coefficient for both the front and rear cylinders, respectively.

Figures 20b–20h show the flow patterns of these seven phases. It can be seen clearly that the fine scales of the flow structures have been properly resolved. The flow from the front cylinder undergoes shear layer instabilities before breaking into vorticities in the wake. The shedding is not apparently strong; thus, the level of the lift coefficient

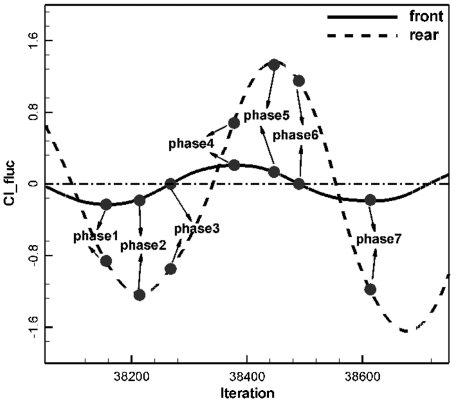

a) Histories of C_L of both cylinders in one period

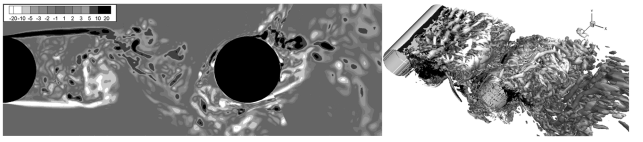

b) Phase 1

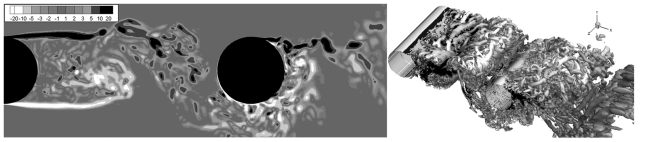

c) Phase 2

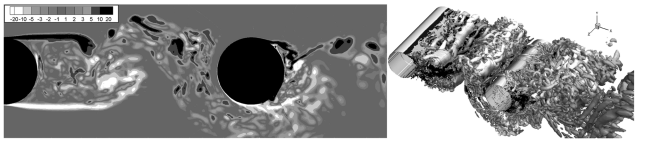

d) Phase 3

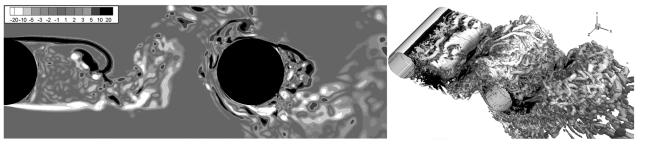

e) Phase 4

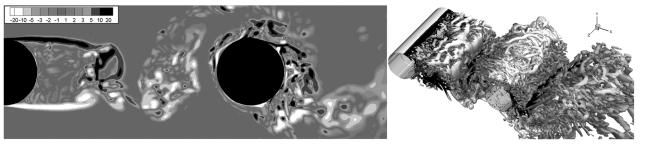

f) Phase 5

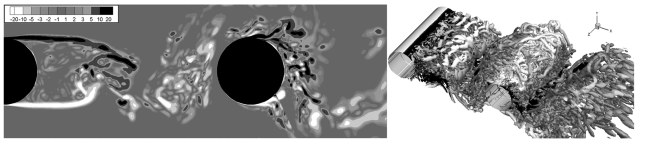

g) Phase 6

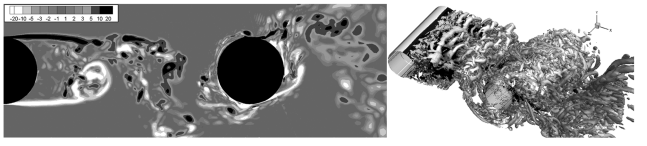

h) Phase 7

Fig. 20 Illustration of the instantaneous flow structures in one typical period defined by the lift coefficient C_L.

for the front cylinder is significantly lower than that for the rear cylinder where vortex impingement and vortex shedding all occur. The flow pattern at the rear cylinder is very complex. Phase 2 and phase 5 are basically skew symmetric, though not in the exact sense for the instantaneous pictures, with vortex shedding occurring from either the lower or upper side of the rear cylinder giving minimum/maximum lift, respectively. At a different phase, such as phase 4, strong vortex impingement on the rear cylinder is evident.

VI. Conclusions

The original Roe scheme with MUSCL interpolation and two S6WENO5 schemes with constant ($\phi = 0.12$) and adaptive dissipation have been implemented together with DDES to study the unsteady and massive separation flow around the TC.

First, the parameter of C_{DES} is recalibrated through simulating DIT using our in-house code UNITs. Four spatial schemes, original Roe, original S6WENO5 and S6WENO5 with 12% dissipation, and fourth-order central schemes, are applied to investigate the effect of numerical dissipation on the turbulence energy spectra. The results show that the original Roe scheme is the most dissipative scheme here; S6WENO5 is better; S6WENO5 with 12% dissipation further improved; and the fourth-order central scheme has the least dissipation and performs best. We can thus conclude the following:

1) The upwind original Roe scheme with limiter and entropy fix is not appropriate for the computation of DIT; it suppresses severely the growth of isotropic turbulence structures. If both limiter and entropy fix are turned off, it performs much better.

2) The S6WENO5 scheme with the original dissipation underpredicts the DIT obviously; its level of dissipation is still high.

3) The S6WENO5 scheme with 12% of original dissipation performs better than original Roe scheme and the original S6WENO5 schemes.

4) The fourth-order central scheme well predicts the DIT and presents the most satisfactory results. Therefore, to accurately predict the high frequency and small scales of turbulent structures, the scheme dissipation should be kept at a minimum level.

5) Fine grid density can perform better, especially using upwind schemes.

Second, the test case of TC is investigated in detail with original Roe scheme, S6WENO5 with 12% dissipation, and S6WENO5 with adaptive dissipation. At the same time, the effects of grid density and spanwise length are also investigated. The following can be concluded:

1) The original Roe scheme is too dissipative to capture the small scale structures. It provides only very large flow structures, like Kármán vortex shedding. It results in much smaller recirculation in the cylinder gap region, larger recirculation behind the rear cylinder, larger $C_{p,\mathrm{rms}}$, and higher PSD on the front cylinder.

2) The C- and A-ϕ schemes can both well resolve most of the mean flow features, such as C_p, velocity, shear layer, $C_{p,\mathrm{rms}}$, and so on. The difference between the two schemes is not distinct. However, they have some distinguishable capability to predict the instantaneous flow futures, such as spanwise vorticity and Q criterion, especially in shear layer. The A-ϕ scheme offers detailed and small scale turbulence structures in the shear layer behind the front cylinder and in the wake of the rear cylinder. The shear layer by A-ϕ appears relatively shorter than that by C-ϕ.

3) The PSDs at sample A and sample B by A-ϕ are in 1 dB difference from the measurement. The frequency difference is about 12 Hz using both A-and C-ϕ schemes.

In summary, DDES coupled with the A-ϕ scheme can be applied to calculate the flow with wide-frequency unsteady and massive separation flows. It can provide detailed instantaneous turbulent structures and sufficiently accurate mean flowfields. The differences between the computations and the measurements are possibly caused by the turbulence simulation model itself.

Acknowledgments

This work was partly supported by the European Union project Advanced Turbulence Simulation for Aerodynamic Application Challenges (contract no. ACP8-GA-2009-233710) and partly supported by the National Science Foundation of China (contracts no. 11072129 and no. 10932005). The authors thank M. Strelets for providing the computational grids of the tandem cylinder and the analysis tools of the decaying isotropic turbulence. Shanghai Supercomputer Center provided most of the computational resources.

References

[1] Lazos, B. S., "Mean Flow Features Around the Inline Wheels of Four-Wheel Landing Gear," *AIAA Journal*, Vol. 40, No. 2, Feb. 2002, pp. 193–198. doi:10.2514/2.1642

[2] Lazos, B. S., "Surface Topology on the Wheels of a Generic Four-Wheel Landing Gear," *AIAA Journal*, Vol. 40, No. 12, Dec. 2002, pp. 2402–2411. doi:10.2514/2.1608

[3] Lazos, B. S., "Reynolds Stresses Around the Wheels of Simplified Four-Wheel Landing Gear," *AIAA Journal*, Vol. 42, No. 1, Jan. 2004, pp. 196–198. doi:10.2514/1.597

[4] Jenkins, L. N., Khorrami, M. R., Choudhari, M. M., and McGinley, C. B., "Characterization of Unsteady Flow Structures Around Tandem Cylinders for Component Interaction Studies in Airframe Noise," AIAA Paper 2005-2812, May 2005.

[5] Jenkins, L. N., Neuhart, D. H., McGinley, C. B., Choudhari, M. M., and Khorrami, M. R., "Measurements of Unsteady Wake Interference Between Tandem Cylinders," AIAA Paper 2006-3202, June 2006.

[6] Neuhart, D. H., Jenkins, L. N., Choudhari, M. M., and Khorrami, M. R., "Measurements of the Flowfield Interaction Between Tandem Cylinders," AIAA Paper 2009-3275, May 2009.

[7] http://cfd.mace.manchester.ac.uk/ATAAC/WebHome [retrieved 26 Feb. 2012].

[8] https://info.aiaa.org/tac/ASG/FDTC/DG/BECAN files/Workshop June 2010 Final problem Statements/Contact Information.pdf [retrieved 26 Feb. 2012].

[9] Lockard, D. P., "Summary of the Tandem Cylinder Solutions from the Benchmark Problems for Airframe Noise Computations 1 Workshop," AIAA Paper 2011-353, Jan. 2011.

[10] Khorrami, M. R., Lockard, D. P., Choudhari, M. M., Jenkins, L. N., Neuhart, D. H., and McGinley, C. B., "Simulations of Bluff Body Flow Interaction for Noise Sources Modeling," AIAA Paper 2006-3203, June 2006.

[11] Lockard, D. P., Khorrami, M. R., Choudhari, M. M., Hutcheson, F. V., and Brooks, T. F., "Tandem Cylinder Noise Predictions," AIAA Paper 2007-3450, May 2007.

[12] Khorrami, M. R., Choudhari, M. M., Lockard, D. P., Jenkins, L. N., and McGinley, C. B., "Unsteady Flowfield Around Tandem Cylinders as Prototype Component Interaction in Airframe Noise," *AIAA Journal*, Vol. 45, No. 8, Aug. 2007, pp. 1930–1941. doi:10.2514/1.23690

[13] Lockard, D. P., Choudhari, M. M., Khorrami, M. R., Neuhart, D. H., Hutcheson, F. V., and Brooks, T. F., "Aeroacoustic Simulations of Tandem Cylinders with Subcritical Spacing," AIAA Paper 2008-2862, May 2008.

[14] Brès, G. A., Wessels, M., and Noelting, S., "Tandem Cylinder Noise Predictions Using Lattice Boltzmann and Ffowcs Williams-Hawkings Methods," AIAA Paper 2010-3791, June 2010.

[15] Brès, G. A., Perot, F., and Freed, D., "A Ffowcs Williams-Hawkings Solver for Lattice-Boltzmann Based Computational Aeroacoustics," AIAA Paper 2010-3711, June 2007.

[16] Weinmann, M., Sandberg, R. D., and Doolan, C. J., "Flow and Noise Predictions for a Tandem Cylinder Configuration Using Novel Hybrid RANS/LES Approaches," AIAA Paper 2010-3787, June 2010.

[17] Spalart, P. R., "Strategies for Turbulence Modeling and Simulations," *International Journal of Heat and Fluid Flow*, Vol. 21, No. 3, June 2000, pp. 252–263. doi:10.1016/S0142-727X(00)00007-2

[18] Spalart, P. R., Jou, W. H., Strelets, M., and Allmaras, S. R., "Comments on the Feasibility of LES for Wings, and on a Hybrid RANS/LES Approach," First AFOSR International Conference on DNS/LES, Ruston, LA, Aug. 1997; also *Advances in DNS/LES*, edited by C. Liu

and Z. Liu, Greyden, Columbus, OH, 1997.
[19] Spalart, P. R., and Allmaras, S. R., "A One-Equation Turbulence Model for Aerodynamic Flows," AIAA Paper 1992-0439, Jan. 1992.
[20] Spalart, P. R., Deck, S., Shur, M., Squares, K., Strelets, M., and Travin, A., "A New Version of Detached Eddy Simulation, Resistant to Ambiguous Grid Densities," *Theoretical and Computational Fluid Dynamics*, Vol. 20, No. 3, May 2006, pp. 181–195. doi:10.1007/s00162-006-0015-0
[21] Shur, M., Spalart, P. R., Strelets, M., and Travin, A., "A Hybrid RANS/LES Approach with Delayed DES and Wall-Modelled LES Capabilities," *International Journal of Heat and Fluid Flow*, Vol. 29, No. 6, Sept. 2008, pp. 1638–1649. doi:10.1016/j.ijheatfluidflow.2008.07.001
[22] Riou, J., Garnier, E., Deck, S., and Basdevant, C., "Improvement of Delayed-Detached Eddy Simulation Applied to Separated Flow Over Missile Fin," *AIAA Journal*, Vol. 47, No. 2, Feb. 2009, pp. 345–360. doi:10.2514/1.37742
[23] Strelets, M., "Detached Eddy Simulation of Massively Separated Flows," AIAA Paper 2001-0879, Jan. 2001.
[24] Menter, F. R., "Two-Equation Eddy-Viscosity Turbulence Models for Engineering Applications," *AIAA Journal*, Vol. 32, No. 8, 1994, pp. 1598–1605. doi:10.2514/3.12149
[25] Menter, F. R., and Kuntz, M., "A Zonal SST-DES Formulation," DES WORKSHOP, St. Petersburg, Russia, July 2003, (http://cfd.me.umist.ac.uk/flomania/index2.html) [retrieved 26 Feb. 2012].
[26] Fu, S., Xiao, Z. X., Chen, H. X., Zhang, Y. F., and Huang, J. B., "Simulation of Wing-Body Junction Flows with Hybrid RANS/LES Methods," *International Journal of Heat and Fluid Flow*, Vol. 28, No. 6, July 2007, pp. 1379–1390. doi:10.1016/j.ijheatfluidflow.2007.05.007
[27] Xiao, Z. X., Chen, H. X., Zhang, Y. F., Huang, J. B., and Fu, S., "Study of Delayed-Detached Eddy Simulation with Weakly Nonlinear Turbulence Model," *Journal of Aircraft*, Vol. 43, No. 5, Sept.–Oct. 2006, pp. 1377–1385. doi:10.2514/1.20127
[28] Xiao, Z. X., and Fu, S., "Studies of the Unsteady Supersonic Base Flows Around Three Afterbodies," *Acta Mechanica Sinica*, Vol. 25, Jan. 2009, pp. 471–479. doi:10.1007/s10409-009-0248-4
[29] Wang, B. Y., Zha, G. C., and Wind, M., "Detached-Eddy Simulation of Transonic Limit Cycle Oscillations Using High Order Schemes," AIAA Paper 2009-1507, Jan. 2009.
[30] Bui, T. T., "A Parallel, Finite-Volume Algorithm for Large-Eddy Simulation of Turbulent Flows," NASA TM-1999-206570, Jan. 1999.
[31] Qin, N., and Xia, H., "Detached Eddy Simulation of a Synthetic Jet for Flow Control," *Proceedings of the Institution of Mechanical Engineers, Part I: Journal of Systems and Control Engineering*, Vol. 222, No. 5, April 2008, pp. 373–380. doi:10.1243/09596518JSCE513
[32] Yoon, S., and Barnhardt, M. D., "Simulations of High-Speed Flow over an Isolated Roughness," AIAA Paper 2010-1573, Jan. 2010.
[33] Travin, A., Shur, M., Strelets, M., and Spalart, P. R., "Physical and Numerical Upgrade in the Detached Eddy Simulation of Complex Turbulence Flows," *Advances in LES of Complex Flows*, edited by R. Friedrich and W. Rodi, Kluwer Academic, Norwell, MA, 2006, pp. 239–254.
[34] Mockett, C., "A Comprehensive Study of Detached-Eddy Simulation," Ph.D. Thesis, Technical University of Berlin, Berlin, 2009.
[35] Jiang, G., and Shu, C. W., "Efficient Implementation of Weighted ENO Schemes," *Journal of Computational Physics*, Vol. 126, No. 1, June 1996, pp. 202–228. doi:10.1006/jcph.1996.0130
[36] Yee, H. C., Sandham, N. D., and Djomehri, M. J., "Low Dissipative High Order Shock-Capturing Methods Using Characteristic-Based Filters," *Journal of Computational Physics*, Vol. 150, No. 1, 1999, pp. 199–238. doi:10.1006/jcph.1998.6177
[37] Usta, E., "Application of a Symmetric Total Variation Diminishing Scheme to Aerodynamic of Rotors," Ph.D. Thesis, Georgia Institute of Technology, Atlanta, 2002.
[38] Xiao, Z. X., Liu, J., Huang, J. B., and Fu, S., "Comparisons of Three Advanced DES Methods on Unsteady Flows past Tandem Cylinders," Fourth Symposium on RANS/LES Hybrid Methods, Beijing, 28–30 Sept. 2011.
[39] Radespiel, R., and Swanson, R. C., "Progress with Multi-Grid Schemes for Hypersonic Flow Problems," NASA CR 189579, 1991.
[40] Comte-Bellot, G., and Corrsin, S., "Simple Eulerian Time Correlation of Full- and Narrow-Band Velocity Signals in Grid-Generated 'Isotropic' Turbulence," *Journal of Fluid Mechanics*, Vol. 48, No. 2, 1971, pp. 273–337. doi:10.1017/S0022112071001599
[41] Jameson, A., Schmidt, W., and Turkel, E., "Numerical Solutions of Euler Equations by Finite Volume Methods with Runge-Kutta Time Stepping Schemes," AIAA Paper 1981-1259, June 1981.

P. Tucker
Associate Editor